Flow, Turbulence and Combustion
https://doi.org/10.1007/s10494-023-00457-8

RESEARCH

Modification of the SSG/LRR-Omega Model for Turbulent Boundary Layer Flows in an Adverse Pressure Gradient

Tobias Knopp[1] · Nico Reuther[2] · Matteo Novara[1] · Daniel Schanz[1] · Erich Schülein[1] · Andreas Schröder[1] · Christian J. Kähler[2]

Received: 20 February 2023 / Accepted: 4 July 2023

Abstract
A modification of the RANS turbulence model SSG/LRR-ω for turbulent boundary layers in an adverse pressure gradient is presented. The modification is based on a wall law for the mean velocity, in which the log law is progressively eroded in an adverse pressure gradient and an extended wall law (designated loosely as a half-power law) emerges above the log law. An augmentation term for the half-power law region is derived from the analysis of the boundary-layer equation for the specific rate of dissipation ω. An extended data structure within the RANS solver provides, for each viscous wall point, the field points on a wall-normal line. This enables the evaluation of characteristic boundary layer parameters for the local activation of the augmentation term. The modification is calibrated using a joint DLR/UniBw turbulent boundary layer experiment. The modified model yields an improved predictive accuracy for flow separation. Finally, the applicability of the modified model to a 3D wing-body configuration is demonstrated.

Keywords RANS turbulence modelling · Adverse pressure gradient · Turbulent boundary layer · Flow separation

1 Introduction

The numerical prediction of turbulent boundary layer (TBL) flows in an adverse pressure gradient (APG) and the onset of flow separation using RANS turbulence models has still not reached the accuracy demands for many technical applications, e.g., for aerodynamics flows around aircraft wings. The computational costs for turbulence resolving simulations are very large for flows at high Reynolds numbers. Moreover, for the configurative design and the optimisation of new aircraft concepts, as well as their certification, a huge number of simulations are needed due to the large parameter space (Reynolds number, Mach number, incidence angle, geometry variations). This will be affordable in the foreseeable future only using RANS-based methods. Improvements of RANS models in the inner part of the boundary layer are also of interest for large-eddy simulation (LES) with wall-functions and hybrid RANS/LES methods based on the detached eddy-simulation approach.

Extended author information available on the last page of the article

The present work is the last step (4.) of an initiative to improve RANS turbulence models for TBLs in an APG involving the following steps:

1. Set-up a database of TBLs in an APG from the literature;
2. Design and provide a joint DLR/UniBw experiment of a TBL in a strong APG at high *Re* for the database (see step 1.) and as a testcase to calibrate RANS turbulence models;
3. Develop an (empirical) wall law for TBLs in an APG;
4. Develop and calibrate a modification for the SSG/LRR-ω model [see Eisfeld et al. (2016)] to account for the wall law in an APG.

The present paper references two previous companion articles. Knopp et al. (2021) describes the DLR/UniBw TBL experiment aiming at (2.) and (3.). In Knopp (2022), a wall law for adverse pressure gradients is devised (3.), using an evaluation of a large data base from the literature (1.) and the DLR/UniBw experiment (2.). The conjecture of a wall law for the mean velocity, which is governed mainly by local parameters, but whose details can be perturbed by higher-order local and history effects, is also discussed in Knopp (2022).

The wall law described in Knopp (2022) is in concurrence with previous findings in the literature. The log law for the mean velocity is found to be a resilient feature in an APG [see Coles and Hirst (1969), Johnstone et al. (2010)]. The region occupied by the log law (in ratio to the boundary layer thickness δ) is found to be progressively reduced as the effect of the APG becomes stronger. Some researchers report, that a half-power law emerges above the log law [see e.g. Brown and Joubert (1969) and Knopp et al. (2021)].

For the RANS turbulence modelling (4.), the approach by Rao and Hassan (1998), Catris and Aupoix (2000) is revisited and applied to modify the ω-equation within the differential Reynolds stress model (DRSM) SSG/LRR-ω. A key idea is to activate the modification only in a certain part of the inner layer, i.e., in the assumed half-power-law region, using suitable blending functions. Preliminary results were given for the SST k–ω model in Knopp (2016) and for the SSG/LRR-ω model in Knopp et al. (2021). In the present work, an alternative formulation for the augmentation term of the ω-equation is proposed, that does not involve the local pressure gradient via the pressure diffusion term, following Spalart (2015). This was inspired by Hanjalic and Launder (1980), proposing the sensitisation of the dissipation equation to irrotational strain. Such turned out to be successful in boundary layer flows in an APG [see also Hanjalic et al. (1999), Apsley and Leschziner (2000), and Probst and Radespiel (2008)], demonstrating the significant effect of the length-scale equation on the overall model behaviour.

There are some indications that popular RANS models (SA, SST, SSG/LRR-ω) predict separation on a smooth surface too far downstream. An example is the HGR01 airfoil at $Re_c = 0.65 \times 10^6$. The RANS models SA, SST, and SSG/LRR-ω were found to predict separation too far downstream for the cases with incipient separation at $\alpha = 11°$ and $\alpha = 12°$ compared to the experimental data by Wokoeck et al. (2006) and the LES results by Geurts et al. (2012) [see Wokoeck et al. (2006) and Probst and Radespiel (2008)]. Similar observations were made for the SST model for the flow around wind-turbine airfoils [see Menter et al. (2018), Menter (2022)] and for the SA model in Medida and Baeder (2013). However, the results are not unambiguous. As an example, for the DNS of a turbulent boundary layer flow with separation and reattachment by Coleman et al. (2018), SA, SST, and SSG/LRR-ω were found to predict separation more upstream than the DNS. As a remedy, the modification of the SSG/LRR-ω model is calibrated in the present work using the joint DLR/UniBw experiment of a TBL in a strong APG at high *Re* [see Knopp et al. (2021)].

The paper is organized as follows. In Sect. 2 the wall law in an APG is described. Next, in Sect. 3 the governing equations of the SSG/LRR-ω model and the modelling assumptions are stated. The behaviour of the ω-equation in an APG is studied in Sect. 4. The modification of the ω-equation is elucidated in Sect. 5. The numerical method is outlined in Sect. 6. The numerical results are presented in Sect. 7 for the DLR/UniBw turbulent boundary layer experiment and in Sect. 8 for the flow around two-dimensional airfoils. The applicability of the method for 3D aircraft configurations is demonstrated in Sect. 9. The conclusions are given in Sect. 10.

2 Wall Law in an Adverse Pressure Gradient

Two-dimensional, incompressible turbulent boundary-layer flow in a wall- and flow-fitted coordinate system is assumed with the streamwise wall-parallel direction s, the wall-normal direction y, the mean-velocity components U (wall-parallel streamwise) and V (wall-normal), and the corresponding fluctuating components u' and v'

$$\nu \frac{\partial^2 U}{\partial y^2} - \frac{\partial \overline{u'v'}}{\partial y} = \frac{1}{\rho}\frac{\mathrm{d}P}{\mathrm{d}s} + U\frac{\partial U}{\partial s} + V\frac{\partial U}{\partial y} + \frac{\partial}{\partial s}\left(\overline{u'^2} - \overline{v'^2}\right). \tag{1}$$

In the three-dimensional case, the direction s is defined by the direction of the wall-parallel velocity as $y \to 0$ (being the direction of the skin friction vector).

2.1 Wall Law for the Mean Velocity

The RANS modification relies on the following hypotheses about an empirical wall law for the mean velocity [see the companion paper Knopp (2022) for details]:

- The log law in the mean velocity is a resilient feature in an APG;
- The log law is progressively eroded in an APG and the outer edge of the log-law region (in ratio to δ) is decreasing with increasing Δp_s^+;
- An extended wall law (designated loosely as "half-power law", abbreviated u^+_{sqrt}) emerges above the log law in a large part of the region (in terms of y/δ) the log law occupies in a TBL at zero pressure gradient ($y/\delta < 0.2$).

The wall law uses inner viscous scaling $u^+ = U/u_\tau$, $y^+ = yu_\tau/\nu$ with the wall shear stress τ_w, the density ρ, the friction velocity $u_\tau = \sqrt{\tau_w/\rho}$, and the kinematic viscosity ν. The structure of the wall law is given by

$$u^+ = \begin{cases} u^+_{\mathrm{log}} & \text{if} \quad y^+ \in (y^+_{\mathrm{log,min}}, y^+_{\mathrm{log,max}}) \\ u^+_{\mathrm{sqrt}} & \text{if} \quad y^+ \in (y^+_{\mathrm{sqrt,min}}, 0.2\delta^+) \end{cases} \tag{2}$$

The locations of the log-law region and of the half-power-law region within the inner layer ($y/\delta < 0.2$) are given, respectively, by the y^+-intervals $(y^+_{\mathrm{log,min}}, y^+_{\mathrm{log,max}})$ and $(y^+_{\mathrm{sqrt,min}}, 0.2\delta^+)$. These are described in Sect. 2.3. The values of the constants in the log law

$$u^+_{\mathrm{log}} = \frac{1}{\kappa}\log(y^+) + B \tag{3}$$

(the von Kármán constant κ and B) are the same as for zero pressure gradient turbulent boundary layer flows. The extended wall law involves the pressure gradient parameter α^+ (α^+ is defined below)

$$u^+_{\mathrm{sqrt}} = \frac{1}{K}\left[2\left((1+\alpha^+y^+)^{\frac{1}{2}}-1\right)+\log(y^+)+2\log\left(\frac{2}{(1+\alpha^+y^+)^{\frac{1}{2}}+1}\right)\right]+B_{\mathrm{o}}. \tag{4}$$

This formula interpolates the log law and the half-power law, respectively, as α^+ tends to zero or to infinity. In the half-power-law region $(y^+_{\mathrm{sqrt,min}}, 0.2\delta^+)$, α^+y^+ is large, and the first term in (4) is the governing term [see below in Fig. 10 (right)]. As the (formal) interpolation between the log law and the half-power law in (4) cannot describe the resilience of the log law below $y^+_{\mathrm{log,max}}$ for large values of Δp^+_s, Eq. (4) is combined with (3) in (2) (see Sect. 7.3). As described below, the value of K is found to be the same as κ. Note that B_{o} is not a constant and is different from B in (3); instead, $B_{\mathrm{o}} = B_{\mathrm{o}}(Re_\tau, \Delta p^+_s)$, as $y^+_{\mathrm{log,max}}$ and $y^+_{\mathrm{sqrt,min}}$ are functions of the local values of $Re_\tau(s) = \delta(s)u_\tau(s)/\nu$ and $\Delta p^+_s(s)$ (see Sect. 2.3). Moreover, note that there is an intermediate region in which neither the log law nor the half-power law describes the mean velocity.

2.2 Theory

The half-power law can be derived from the assumption that the total shear stress τ can be approximated by a linear relation (λ is described below)

$$\tau^+ \equiv \frac{\mathrm{d}u^+}{\mathrm{d}y^+} - \overline{u'v'}^+ = 1+\alpha^+y^+, \quad \alpha^+ \equiv \lambda\,\Delta p^+_s, \quad \Delta p^+_s = \frac{\nu}{\rho u^3_\tau}\frac{\mathrm{d}P}{\mathrm{d}s} \tag{5}$$

in conjunction with the eddy-viscosity hypothesis (using $\nu^+_{\mathrm{t}} = \nu_{\mathrm{t}}/\nu$) [see McDonald (1969)]

$$-\overline{u'v'}^+ = \nu^+_{\mathrm{t}}\frac{\mathrm{d}u^+}{\mathrm{d}y^+} = \left(Ky^+\frac{\mathrm{d}u^+}{\mathrm{d}y^+}\right)^2 = 1+\alpha^+y^+ \quad \Leftrightarrow \quad \frac{\mathrm{d}u^+}{\mathrm{d}y^+} = \frac{\sqrt{1+\alpha^+y^+}}{Ky^+}. \tag{6}$$

Integration of (6) gives (4). In (5), the notation $\tau^+ = \tau/\tau_{\mathrm{w}}$ and $\overline{u'v'}^+ = \overline{u'v'}/u^2_\tau$ is used. As described in Knopp (2022), Eq. (5) can be seen as a first-order approximation of the relation

$$\frac{\partial\tau^+}{\partial y^+} = \Delta p^+_s + \text{H.O. local terms} + \text{History effects}. \tag{7}$$

The higher order (H.O.) local terms involve the wall-shear-stress-gradient parameter $\Delta u^+_{\tau,s} = \nu u^{-2}_\tau \mathrm{d}u_\tau/\mathrm{d}s$ (describing the relative importance of the mean-inertia term) and a parameter involving $\mathrm{d}^2P/\mathrm{d}s^2$. Therefore, α^+ is an approximation of $\partial\tau^+/\partial y^+$. The results in McDonald (1969) and Knopp et al. (2015) indicate that $\lambda = 0.9$ for flows close to equilibrium and $\lambda = 0.7$ for streamwise evolving flows.

Note that (4) gives for large $\Delta p^+_s y^+$ (for strong pressure gradients, say $\Delta p^+_s > 0.01$, and large y^+-values reached in high-Re flows) and as the flow approaches separation ($u_\tau \to 0$)

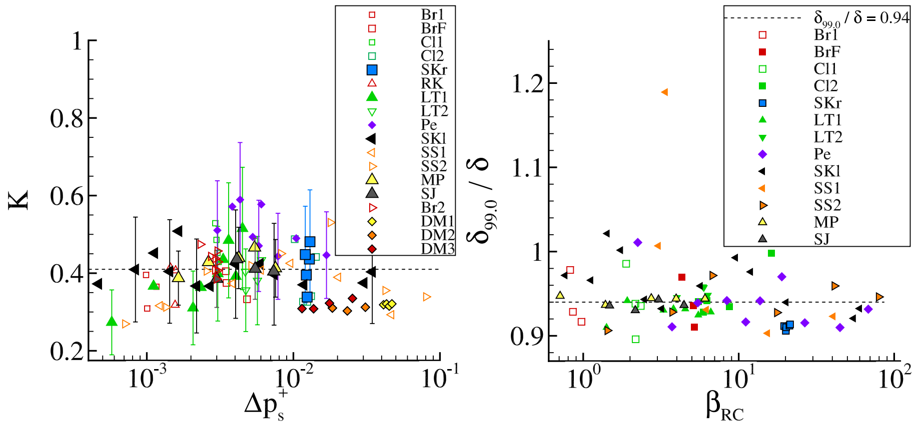

Fig. 1 Slope coefficient K of the half-power law (left) using large filled symbols to highlight the data sets used for the calibration and ratio of δ_{99}/δ (right)

$$U(y) = \frac{2}{K}\sqrt{\lambda \frac{1}{\rho}\frac{\mathrm{d}P}{\mathrm{d}s} y} \tag{8}$$

which was inferred in Stratford (1959) for a flow with exactly zero skin friction, with K sometimes referred to as the "Stratford constant". In a flow with $\tau_\mathrm{w} \equiv 0$, Eqs. (1) and (7) imply that $\lambda \equiv 1$ [see also Stratford (1959)].

2.3 Calibration

The calibration of the wall law involves the coefficient K and the transition from the log law to the half-power law, which is described by empirical correlations for $y^+_{\mathrm{log,max}}$ and $y^+_{\mathrm{sqrt,min}}$.

The calibration of K in (4) uses the evaluation of a database of turbulent boundary layer flows in an APG described in Knopp (2022), which is summarised in table 1. For each mean-velocity profile of the database, the value for K was determined by a least-squares fit of (4) to the experimental mean-velocity profile in the supposed region of the half-power law. The value of K depends on the choice for α^+ in (4). The present work uses $\lambda = 0.9$ for equilibrium flows and $\lambda = 0.7$ for streamwise evolving flows to account for the modelling assumption $\alpha^+ \approx \partial\tau^+/\partial y^+$. The data sets used for the calibration (SKr, SKl, MP, SJ, LT1) are plotted using large filled symbols [see Knopp (2022)]. The data sets by Perry and the DLR/UniBw experiments are plotted using small filled symbols and are considered at a lower priority, due to supposed history effects. The other data sets are not used for the calibration and are plotted using open symbols. The data points are found to spread around $K = 0.41$ [see Fig. 1(left)]. Note that $K = 0.45$ was found using $\lambda = 1$ for all flows in Knopp (2022) aiming at the comparison with other results for K in the literature.

The spreading in K in the range of 0.27 to 0.58 needs to be discussed. Most data points for K are in the range of 0.31 to 0.51. On the one hand, the uncertainty bars are large (in the range of 18% to 33% due to the different sources of uncertainties). Note that the uncertainties are quantified and discussed in section 6.5 and in the appendix of the companion paper Knopp (2022). The spreading of the data around $K = 0.41$ occurs mostly within the

Table 1 Summary of the data evaluation and the acronyms used in the figure legends

Acro-nym	Author(s)[1]	Val. for λ	Used for calibr. of K
Br1	Bradshaw, mild	0.9	−
BrF	Bradshaw & Ferriss	0.9	−
Cl1	Clauser, mild	0.9	−
Cl2	Clauser, moderate	0.9	−
LT1	Ludwieg & Tillmann, mild	0.7	+
LT2	Ludwieg & Tillmann, strong	0.7	−
Pe	Perry	0.7	−
SKl	Schubauer & Klebanoff	0.7	+
SS1	Schubauer & Spangenberg, B	0.7	−
SS2	Schubauer & Spangenberg, E	0.7	−
Br2	Bradshaw	0.9	−
SJ	Samuel & Joubert	0.7	+
MP	Marusic & Perry	0.7	+
SKr	Skare & Krogstad	0.9	+
RK	Romero & Klewicki (UNH)	0.7	−
DM1	DLR/UniBw I	0.7	−
DM2	DLR/UniBw II 23 m/s	0.7	−
DM3	DLR/UniBw II 36 m/s	0.7	−

[1]The acronyms and references are the same as in the companion paper Knopp (2022)

uncertainty bars. On the other hand, the variability of K is supposed to be attributed to both higher-order local and history effects, which are discussed in section 7.2 in Knopp (2022). Higher-order local effects are the mean flow acceleration described by the parameter $\Delta u^+_{\tau,s}$, and the effects of an increasing or decreasing APG depending on $\mathrm{d}^2P/\mathrm{d}s^2$. Such effects are not accounted for, if a constant value of K is used. The present model only accounts for the overall effect of an APG.

Regarding the half-power law (8) for a turbulent boundary layer flow with zero skin friction, Stratford reported a value of $K = 0.66\kappa = 0.27$ for his zero skin friction flow. For the same data, Townsend (1960) found $K = 0.5 \pm 0.05$, whereas Mellor (1966) found that, at most, $K = 0.44$ by excluding certain near wall points. Therefore, Eq. (4) and the calibration of K are in concurrence with the Stratford limit of zero skin friction flow. Note that, in the present work, B_o is not needed, as only (6) will be employed for the modelling, but not (4).

The quantity $y^+_{\mathrm{log,max}}$ defines the y^+-location of the outer edge of the log-law region, describing the progressive erosion of the log-law region in an APG. Similarly, $y^+_{\mathrm{sqrt,min}}$ describes the y^+-location above which the half-power law emerges. For both quantities, an empirical correlation was proposed in the companion paper Knopp (2022) from the evaluation of a database of different TBL flows in an APG (see table 1). The empirical correlations are functions of Δp^+_s and of the local Reynolds number $Re_\tau = \delta u_\tau/\nu$

$$y^+_{\mathrm{log,max}} = 1.68 Re_\tau^{1/2}\,(\Delta p^+_s)^{-1/5}, \quad y^+_{\mathrm{sqrt,min}} = 4.05 Re_\tau^{1/2}\,(\Delta p^+_s)^{-0.13}. \tag{9}$$

Note that Re_τ involves the local boundary layer thickness δ. The correlations were found using similarity and scaling arguments [see section 6.1 in Knopp (2022)]. The *Re*-dependence of the mean-velocity profile due to (9) is in agreement with the findings by Klewicki et al. (2009) for TBLs in zero pressure gradient and by Yaglom (1979) for TBLs in an APG. The definition used to determine $y^+_{\rm log,max}$ and $y^+_{\rm sqrt,min}$ from the database is given in section 4.2 in Knopp (2022). It is noteworthy that (9) accounts for the overall effect of an APG, but not for higher-order local effects and history effects in complex pressure gradients.

For the determination of δ within a RANS solver, the quantity δ_{99} is used, being the wall distance y, where $U(y) = 0.99U_e$ (U_e is the boundary layer edge velocity). The evaluation of the mean-velocity profiles of the database shows that the ratio δ_{99}/δ is spreading around a constant value over a large range of pressure gradients, given here in the scaling by Rotta and Clauser $\beta_{RC} = (\delta^*/\tau_w)(\mathrm{d}P/\mathrm{d}s)$ with δ^* being the displacement thickness. The boundary layer thickness δ was determined by a fit of the mean-velocity profiles to the law-of-the-wall/law-of-the-wake [see Coles and Hirst (1969), Knopp (2022)]. A value of $\delta_{99} = 0.94\delta$ is inferred from Fig. 1 (right) as an approximation. Note that $\delta_{99.5} = 0.98\delta$ was found in Knopp (2022), but $\delta_{99} \equiv \delta_{99.0}$ was observed to be more robust for flows around airfoils than $\delta_{99.5}$.

3 Governing Equations and Modelling

The SSG/LRR-ω model by Eisfeld et al. (2016) is used as the starting point for the present modification for turbulent boundary layers in an APG.

3.1 The SSG/LRR-ω Model

The equation for the Reynolds stresses $\overline{u_i'u_j'}$ is written in the form

$$\frac{\partial \overline{u_i'u_j'}}{\partial t} + \frac{\partial}{\partial x_k}\left(U_k \overline{u_i'u_j'}\right) = P_{ij} + \Pi_{ij} - \epsilon_{ij} + D^\nu_{ij} + D^t_{ij} + D^p_{ij}. \tag{10}$$

$P_{ij} = -\overline{u_i'u_k'}(\partial U_j/\partial x_k) - \overline{u_j'u_k'}(\partial U_i/\partial x_k)$ denotes production, Π_{ij} is the pressure-strain correlation tensor, and $\epsilon_{ij} = (2/3)\epsilon\delta_{ij}$ is the dissipation tensor. Here δ_{ij} is the Kronecker-delta, $\epsilon = C_\mu k\omega$, $k = \overline{u_i'u_i'}/2$ is the turbulent kinetic energy. D^ν_{ij} and D^t_{ij} denote viscous and turbulent transport, and D^p_{ij} denotes the transport due to pressure fluctuations (or: pressure diffusion). The present work uses the so-called SSGLRR-RSM-w2012,[1] which employs a generalized gradient diffusion model for D^t_{ij} (neglecting D^p_{ij}). Note that equation (10) remains unaltered in the present work.

The baseline ω-equation used in the SSG/LRR-ω model is

$$\frac{\partial \omega}{\partial t} + \frac{\partial}{\partial x_j}\left(U_j\omega\right) - D^\nu_\omega - D^t_\omega - D^p_\omega = P_\omega - \epsilon_\omega + D_{\rm cd} \tag{11}$$

[1] https://turbmodels.larc.nasa.gov/rsm-ssglrr.html.

with production $P_\omega = (\gamma\omega/k)P_k$ (P_k is the production of k and given by $P_k = -\overline{u_i'u_j'}\partial U_i/\partial x_j = P_{ii}/2$) and dissipation $\epsilon_\omega = \beta_\omega \omega^2$. Note that $\gamma \equiv \alpha_\omega$ in the notation used in Eisfeld et al. (2016). The sum of the turbulent transport due to velocity fluctuations D^t_ω and due to pressure fluctuations D^p_ω is modelled using a gradient-diffusion hypothesis

$$-D^t_\omega - D^p_\omega = -\frac{\partial}{\partial x_j}\left(\sigma_\omega \frac{k}{\omega}\frac{\partial \omega}{\partial x_j}\right) \tag{12}$$

The viscous transport D^ν_ω and the cross-diffusion term D_{cd} are defined by

$$-D^\nu_\omega = -\frac{\partial}{\partial x_j}\left(\nu \frac{\partial \omega}{\partial x_j}\right), \quad D_{\mathrm{cd}} = \frac{\sigma_d}{\omega}\max\left(\frac{\partial k}{\partial x_j}\frac{\partial \omega}{\partial x_j}, 0\right) \tag{13}$$

All the coefficients are blended between inner and outer part of the boundary layer using the blending function F_1 [see Menter (1993), Eisfeld et al. (2016)]. The term D_{cd} is not active in the inner layer of a TBL as $\sigma_d = 0$ due to the blending function F_1.

3.2 Boundary Layer Approximation

The following boundary layer approximations for the ω-equation are made: (i) the convection of ω can be neglected; (ii) the derivatives in the wall-normal direction are much larger than in the streamwise and spanwise direction; (iii) the viscous transport of ω can be neglected in the region $y^+ > y^+_{\mathrm{log,min}}$. Using $\nu_t = k/\omega$ and inner scaling for the turbulence quantities

$$-\overline{u'v'}^+ = \frac{-\overline{u'v'}}{u_\tau^2}, \quad k^+ \equiv \frac{k}{u_\tau^2}, \quad \nu_t^+ = \frac{\nu_t}{\nu}, \quad \omega^+ \equiv \frac{\omega}{\nu u_\tau^2}, \tag{14}$$

the boundary layer approximation for the ω-equation becomes

$$-D^{t,+}_{\omega,\mathrm{bl}} - D^{p,+}_{\omega,\mathrm{bl}} = P^+_{\omega,\mathrm{bl}} - \epsilon^+_{\omega,\mathrm{bl}} + D^+_{\mathrm{cd,bl}} \tag{15}$$

with the notation

$$P^+_{\omega,\mathrm{bl}} = -\gamma\frac{\omega^+}{k^+}\frac{\mathrm{d}u^+}{\mathrm{d}y^+}\overline{u'v'}^+, \qquad \epsilon^+_{\omega,\mathrm{bl}} = \beta_\omega\left(\omega^+\right)^2,$$
$$-D^{t,+}_{\omega,\mathrm{bl}} - D^{p,+}_{\omega,\mathrm{bl}} = -\frac{\mathrm{d}}{\mathrm{d}y^+}\left(\sigma_\omega \nu_t^+ \frac{\mathrm{d}\omega^+}{\mathrm{d}y^+}\right), \quad D^+_{\mathrm{cd,bl}} = \frac{\sigma_d}{\omega^+}\max\left(\frac{\mathrm{d}k^+}{\mathrm{d}y^+}\frac{\mathrm{d}\omega^+}{\mathrm{d}y^+}, 0\right).$$

3.3 Modelling Assumptions

For the analysis, additionally the turbulent viscosity assumption is used, as well as a relation for $|\overline{u'v'}^+|/k^+$ similar to the Bradshaw hypothesis [see p. 135 in Durbin and Reif (2001) and equation (16) in Menter (1993)]

$$-\overline{u'v'}^+ = \nu_t^+\frac{\mathrm{d}u^+}{\mathrm{d}y^+}, \qquad \nu_t^+ = \frac{k^+}{\omega^+}, \quad \frac{-\overline{u'v'}^+}{k^+} = a_{12}. \tag{16}$$

Here, a_{12} is assumed to be approximately constant for $y^+_{\log,\min} < y^+ < 0.2\delta^+_{99}$ along a given wall-normal line with $a_{12} = 0.3 = \sqrt{C_\mu}$, but a_{12} could be varying slowly. Then, $\omega^+ = a_{12}^{-1}\mathrm{d}u^+/\mathrm{d}y^+$ follows from (16). Note that (16) is needed only for the analysis to relate ω^+ to $|\overline{u'v'}^+|$ and $\mathrm{d}u^+/\mathrm{d}y^+$. In particular, Eq. (16) does not bypass the constitutive relation of a DRSM by introducing the Boussinesq hypothesis. This is explained in Sect. 5.5.

3.4 Boundary Layer Solution in an APG

From the assumed wall law for the mean velocity (3), (6) and for the turbulent shear stress (5) in conjunction with the relations described in Sect. 3.3, the solution for u^+, $\overline{u'v'}^+$, k^+, and ω^+ in the log-law region and in the half-power law region can be inferred.

3.4.1 Solution in the Log-Law Region in an APG

In the log-law region in an APG, Eqs. (3), (5) and (16) imply that

$$\frac{\mathrm{d}u^+}{\mathrm{d}y^+} = \frac{1}{\kappa y^+}, \quad -\overline{u'v'}^+ = 1 + \alpha^+ y^+, \quad \nu_t^+ = \frac{-\overline{u'v'}^+}{\mathrm{d}u^+/\mathrm{d}y^+} = \kappa y^+(1 + \alpha^+ y^+). \tag{17}$$

Then the solutions for k^+ and ω^+ become

$$k^+ = \frac{1 + \alpha^+ y^+}{a_{12}}, \quad \omega^+ = \frac{k^+}{\nu_t^+} = \frac{1}{a_{12}} \frac{1}{\kappa y^+}. \tag{18}$$

3.4.2 Solution in the Half-Power Law Region in an APG

In the half-power law region in an APG, Eqs. (6) and (5) imply that

$$\frac{\mathrm{d}u^+}{\mathrm{d}y^+} = \frac{\sqrt{1 + \alpha^+ y^+}}{K y^+}, \quad -\overline{u'v'}^+ = 1 + \alpha^+ y^+, \quad \nu_\mathrm{t}^+ = K y^+ \sqrt{1 + \alpha^+ y^+}. \tag{19}$$

Then the solutions for k^+ and ω^+ become

$$k^+ = \frac{1 + \alpha^+ y^+}{a_{12}}, \quad \omega^+ = \frac{k^+}{\nu_t^+} = \frac{\sqrt{1 + \alpha^+ y^+}}{a_{12} K y^+}. \tag{20}$$

4 Study of the ω-Equation in an APG

A guiding idea of the present approach is the claim that a RANS turbulence model should be consistent with respect to the assumed boundary layer solution, i. e., the assumed solution should solve the boundary-layer equation for ω. The approach follows the work by Rao and Hassan (1998) and consists of the following steps:

1. Derive a suitable BL equation for ω, scaled to plus units (see (15));

2. Make an assumption for the solution for u^+, k^+, $\overline{u'v'}^+$, and ω^+;
3. Substitute the assumed solution into the ω-equation, and check if the ω-equation is satisfied. Otherwise an unbalanced remainder term is obtained, i.e., a model discrepancy term, denoted by m^+_ω;
4. Express m^+_ω using suitable mean-flow gradient and turbulence quantities. This provides the model augmentation term, which, if added to the ω-equation, makes the equation consistent with the assumed solution;
5. Re-scale the augmentation term to dimensional units;
6. Generalize the augmentation term for three-dimensional flows;
7. Design blending functions for the local activation of the augmentation term.

The steps 1 and 2 were already accomplished in the previous section. Step 3 will be the subject of this section. The steps 4–7 will be the topic of Sect. 5. Note that the approach is sometimes called the 'method of manufactured solutions'.

4.1 Analysis of the Log-Law Region in an APG

First the log-law region is considered. The assumed solution (17)–(18) for u^+, k^+ and ω^+ is substituted into the ω-equation. Note that $D^+_{\mathrm{cd,bl}} = 0$ in (15) as $(\mathrm{d}k^+/\mathrm{d}y^+)(\mathrm{d}\omega^+/\mathrm{d}y^+) < 0$ and $\sigma_d = 0$ due to F_1. This yields

$$-D^{t,+}_{\omega,\mathrm{bl}} - D^{p,+}_{\omega,\mathrm{bl}} = P^+_{\omega,\mathrm{bl}} - \epsilon^+_{\omega,\mathrm{bl}} \quad \Leftrightarrow \quad -\frac{\sigma_\omega}{a_{12}} \frac{1}{(y^+)^2} = \left(\gamma - \frac{\beta_\omega}{a_{12}}\right) \frac{1}{(\kappa y^+)^2} \tag{21}$$

The left hand side and the right hand side of this equation are equal if $a_{12} = C_\mu^{-1/2}$, due to the calibration relation for the log law at ZPG

$$-\frac{\sigma_\omega}{a_{12}} = \frac{1}{\kappa^2}\left(\gamma - \frac{\beta_\omega}{a_{12}^2}\right). \tag{22}$$

The conclusion is that the ω-equation without the cross-diffuson term is consistent with the assumed solution in the log-law region in an APG.

Note that the basic cross-diffusion term without the max-form

$$D^+_{\mathrm{cd}} = \frac{\sigma_d}{\omega^+} \frac{\mathrm{d}k^+}{\mathrm{d}y^+} \frac{\mathrm{d}\omega^+}{\mathrm{d}y^+} = -\frac{\sigma_d}{a_{12}} \frac{\alpha^+}{y^+}$$

is not zero in the case of an APG. Including a cross-diffusion term in the log-law region would deteriorate the log-law behaviour in an APG. In order to avoid confusion, recall that the cross-diffusion term is zero in the inner layer for the SSG/LRR-ω model (as explained above).

However, a cross-diffusion term arises if the ω-equation is obtained from the ϵ -equation by a variable transformation [see Pope (2000)]. This cross-diffusion term could contribute to the overall tendency of the standard k–ϵ model to predict separation on a smooth surface due to an APG more downstream than k–ω type models. To see this, an additional term $D_{\mathrm{cd}} < 0$ in (11) would cause smaller values for ω and hence for ϵ in (10), and therefore a larger mixing of momentum, due to increased values for $\overline{u'v'}$.

This could explain, in part, the need to modify the ϵ-equation in an APG [see e.g. Hanjalic and Launder (1980), Hanjalic et al. (1999), Probst and Radespiel (2008)].

4.2 Analysis of the Half-Power Law Region in an APG

Next, the half-power law region is considered. The assumed solution (19)–(20) is substituted into the ω-equation. Note that $D^{+}_{\mathrm{cd,bl}} = 0$ in (15) as $(\mathrm{d}k^+/\mathrm{d}y^+)(\mathrm{d}\omega^+/\mathrm{d}y^+) < 0$ and $\sigma_d = 0$ due to F_1. Then (15) becomes

$$-D^{t,+}_{\omega,\mathrm{bl}} - D^{p,+}_{\omega,\mathrm{bl}} = P^{+}_{\omega,\mathrm{bl}} - \epsilon^{+}_{\omega,\mathrm{bl}} \quad \Leftrightarrow \quad -\frac{\sigma_\omega}{a_{12}} \frac{1}{(y^+)^2} = \left(\gamma - \frac{\beta_\omega}{a_{12}^2}\right) \frac{1 + \alpha^+ y^+}{(K y^+)^2} \tag{23}$$

This equation is satisfied only if $\alpha^+ = 0$ and $K = \kappa$. The latter condition is indeed fulfilled from the results in Fig. 1(left). Otherwise, the calibration relation (22) for γ needs to be altered, based on K instead of κ. Regarding the first condition, if $\alpha^+ > 0$, then the ω-equation is not consistent with the assumed solution in the half-power law region in an APG. The model discrepancy term m^+_ω for the 1/2-power layer is inferred from (23), which, if added to the ω-equation, makes the ω-equation consistent with the assumed solution

$$-D^{t,+}_{\omega,\mathrm{bl}} - D^{p,+}_{\omega,\mathrm{bl}} = P^{+}_{\omega,\mathrm{bl}} - \epsilon^{+}_{\omega,\mathrm{bl}} + m^{+}_{\omega,\mathrm{bl}}, \qquad m^{+}_{\omega,\mathrm{bl}} = \frac{\gamma}{2K^2} \frac{\alpha^+}{y^+}. \tag{24}$$

Note that the relation $\gamma - \beta_\omega a_{12}^{-2} = -\gamma/2$ for SST and SSG/LRR-ω was used in the last equation, and that $m^{+}_{\omega,\mathrm{bl}}$ is found to be positive in an APG. This equation gives the spatial discrepancy term $m^{+}_{\omega,\mathrm{bl}}$ in boundary layer form as an analytical function of y^+ and α^+. The observation that the half-power law is not a solution to the k–ω and k–ϵ models is cited in Durbin and Reif (2001) as problem 6.14.

The basic cross-diffusion term without the max-term becomes (after substitution of the half-power law solution)

$$D^{\omega,+}_{\mathrm{cd,bl}} = -\frac{\sigma_d}{a_{12}} \frac{\alpha^+\left(1 + \frac{1}{2}\alpha^+ y^+\right)}{(1 + \alpha y^+) y^+}. \tag{25}$$

If the cross-diffusion term is included in the inner layer, then the model discrepancy term is increased in an APG, since the cross-diffusion term is negative. This could be an alternative explanation (at least in part) for the observation that the k–ϵ model is found to predict separation more downstream than the k–ω model [see Wilcox (1998)].

4.3 Interim Summary

The analysis of the boundary-layer equations in an APG shows that the solution for u^+, k^+, and ω^+ solves the ω-equation in the log-law region, but that an unbalanced remainder term arises in the half-power law region. This implies that the ω-equation needs to be modified in the half-power law region.

5 Modification of the ω-Equation in an APG

This section describes the steps 4–7 for the modification of the ω-equation.

5.1 Modified Production Term for ω in an APG

The aim is to approximate the discrepancy term m_ω^+ by a term with (approximately) the same functional dependency on y^+ and α^+ using admissible mean-flow gradient and turbulence quantities (step 4). First the idea in Knopp (2016), Knopp et al. (2021) was to use a pressure-diffusion term, originally proposed for the k-equation by Rao and Hassan (1998). Here, an alternative approach is used, inspired by Hanjalic and Launder (1980), to remedy the explicit use of the mean pressure gradient.

Consider the ω-equation with an additional production term $P_{\omega,4} = C_{\omega 4} P_\omega$

$$-D_{\omega,\mathrm{bl}}^{t,+} - D_{\omega,\mathrm{bl}}^{p,+} = P_{\omega,\mathrm{bl}}^+ + P_{\omega,4,\mathrm{bl}}^+ - \epsilon_{\omega,\mathrm{bl}}^+ \tag{26}$$

The additional term has the following approximate behaviour in an APG

$$P_{\omega,4,\mathrm{bl}}^+ \equiv -C_{\omega 4} \gamma \frac{\omega^+}{k^+} \overline{u'v'}^+ \frac{\mathrm{d}u^+}{\mathrm{d}y^+} = C_{\omega 4} \gamma \frac{1 + \alpha^+ y^+}{(\mathcal{K} y^+)^2} \approx C_{\omega 4} \gamma \frac{\alpha^+}{\mathcal{K}^2 y^+}. \tag{27}$$

Then (24) in conjunction with (27) implies that $C_{\omega 4} = 0.5$.

There is an ambiguity in the modelling of m_ω^+. The term before the last approximation in (27) could be interpreted as $m_\omega^+ = C(\mathrm{d}u^+/\mathrm{d}y^+)^2$. Moreover, as ω^+ and $\mathrm{d}u^+/\mathrm{d}y^+$ are proportional in the half-power layer ($\omega^+ = a_{12}^{-1} \mathrm{d}u^+/\mathrm{d}y^+$), possible alternative options could have been $m_\omega^+ = C(\omega^+)^2$ or $m_\omega^+ = C(\mathrm{d}u^+/\mathrm{d}y^+)\omega^+$. The present choice was mainly to be in line with (22) and the calibration of κ (and hence $\mathrm{d}u^+/\mathrm{d}y^+$) in a TBL at ZPG. Note that a_{12} does not appear in (27) to model m_ω^+. Otherwise, a discussion of the calibration due to (16) would be needed (see Sect. 5.5).

5.2 Blending Function for the Half-Power Law Region

The modification of the ω-equation should be activated only in the half-power law region. This is achieved by using the product of two blending functions. The first function f_{b2} is zero in the near wall-region and almost zero in the log-law region, and increases to a value of unity in the half-power law region

$$f_{b2} = 0.5(\tanh(\zeta) + 1), \quad \zeta = \frac{y^+ - y_{\mathrm{incpt}}^+}{c_{b2}(c_{s2}^{-1} y_{\mathrm{sqrt,min}}^+ - c_{s2} y_{\mathrm{log,max}}^+)} \tag{28}$$

with $c_{b2} = 0.5$, $c_{s2} = 1.04$ and $y_{\mathrm{incpt}}^+ = 0.5(y_{\mathrm{log,max}}^+ + y_{\mathrm{sqrt,min}}^+)$. The coefficient c_{b2} controls the slope in the transition region. The value $c_{b2} = 0.5$ yields a less steep gradient in the transition region to facilitate mesh converged solutions on coarser meshes compared to $c_{b2} = 0.2$, which would better shield the log-law region. The graph of f_{b2} is plotted in Fig. 2(left) for two values of Δp_s^+ at $Re_\tau = 7000$.

The second blending function f_{b3} is used to deactivate the modification above the outer edge of the half-power law region

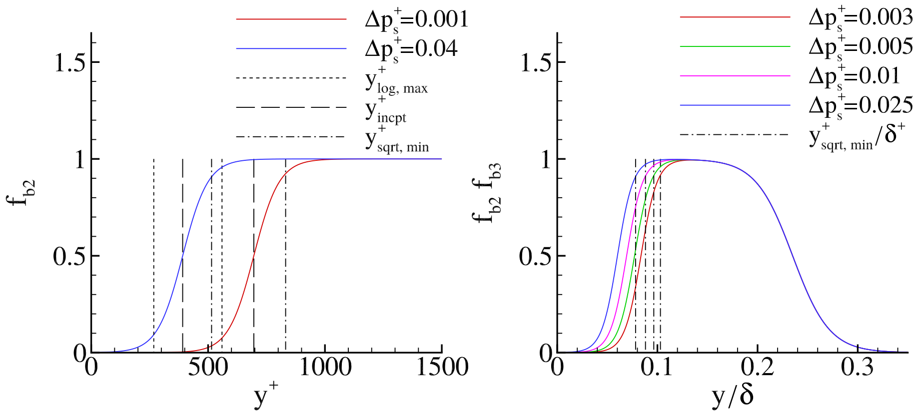

Fig. 2 Blending function f_{b2} for $Re_\tau = 7000$ (left) and $f_{b2}f_{b3}$ for $Re_\tau = 7500$ (right)

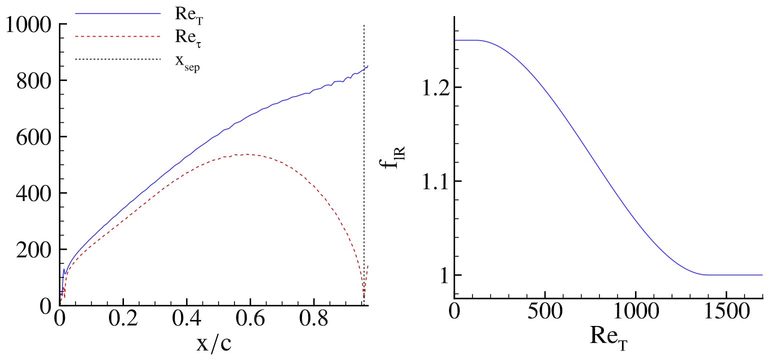

Fig. 3 Left: Re_T and Re_τ for the flow around the HGR01 airfoil at $Re_c = 0.65 \times 10^6$ and $\alpha = 12°$. Right: Modification of the blending function f_{b3} using f_{lR} for small Re

$$f_{b3} = 1 - 0.5(\tanh(\xi) + 1), \quad \xi = \frac{\eta - \eta_{m3}}{c_{b3}(\eta_{u3} - \eta_{l3})}, \quad \eta = \frac{y}{\delta} \tag{29}$$

with the constants $\eta_{l3} = 0.2$, $\eta_{u3} = 0.27$, $\eta_{m3} = 0.5(\eta_{l3} + \eta_{u3})$, and $c_{b3} = 0.525$. Note that $f_{b3} \approx 1$ for $y/\delta < \eta_{l3}$ and $f_{b3} \approx 0$ for $y/\delta > \eta_{u3}$. The slope is controlled by c_{b3}. Note that $\delta = \delta_{99}/0.94$ is applied (see Sect. 2). The region for activating the half-power law modification is given by the product $f_{b2}f_{b3}$. Figure 2(right) shows $f_{b2}f_{b3}$ for $Re_\tau = 7500$.

In a ZPG, the log law in the mean velocity remains unaltered because the blending function is identically zero. For very mild APG, the blending function in the inner layer remains close to zero, as (9) implies that $y^+_{\mathrm{log,max}} > 0.2Re_\tau$ for small Δp_s^+, and hence $f_{b2}f_{b3} \approx 0$.

5.3 Modification for Flows at Small *Re*

A modification of the blending function is applied if the turbulent boundary layer is at a small local Reynolds number Re_T. Here, $Re_T = u_T\delta/\nu$ is used (based on u_T) rather than Re_τ, as $u_\tau \to 0$ and hence $Re_\tau \to 0$, if the flow approaches separation. The modified velocity scale u_T is close to u_τ for small values of Δp_s^+, and $u_T \to 12^{1/3} u_p$ with $u_p = |\nu/\rho \,\mathrm{d}P/\mathrm{d}s|$ as the flow approaches separation (the full definition of u_T is given in section 2.4 in Knopp (2022)). Figure 3(left) provides some illustration.

The modification of (29) for small Re_T (denoted by "low Re", abbreviated lR) increases the outer edge of the half-power law region controlled by f_{b3} by multiplication of η_{l3}, η_{m3} and η_{u3} (given below (29)) with a function $f_{lR}(Re_{T,99})$. To this end, f_{b3} in (29) is replaced by $f_{b3,lR}$

$$f_{b3,lR}(\eta, Re_{T,99}) = 1 - 0.5(\tanh(\xi) + 1), \quad \xi = \frac{\eta - f_{lR}(Re_{T,99})\eta_{m3}}{c_{b3} f_{lR}(Re_{T,99})(\eta_{u3} - \eta_{l3})}, \tag{30}$$

with $\eta = y/\delta$. Note that the blending function is based on $Re_{T,99} = u_T \delta_{99}/\nu$ (using δ_{99} instead of δ). The function f_{lR} leaves f_{b3} unaltered ($f_{lR} = 1.0$) for $Re_{T,99} \geq Re_{T,u}$ with $Re_{T,u} = 1400$. For $Re_{T,99} \leq Re_{T,l} = 120$, f_{b3} is increased, as $f_{lR} = c_{lR} = 1.25$. A smooth interpolation is used in between

$$f_{lR}(Re_{T,99}) = 1 + (c_{lR} - 1)\left[1 - (3\psi^2 - 2\psi^3)\right], \quad \psi = \frac{Re_{T,99} - Re_{T,l}}{Re_{T,u} - Re_{T,l}}. \tag{31}$$

The function f_{lR} is depicted in Fig. 3(right). The reason for the modification is that the maximum of $f_{b2} f_{b3}$ can be significantly smaller than one for flows at a small Re_T despite relevant values of Δp_s^+.

5.4 Summary of the Modified ω-Equation

The modified ω-equation with the APG modification term $P_{\omega,4}$, the damping functions f_{b2}, $f_{b3,lR}$ defined in (28), (30), and an additional activation function χ becomes

$$\frac{\partial \omega}{\partial t} + \frac{\partial}{\partial x_j}\left(U_j \omega\right) - D_\omega^\nu - D_\omega^t - D_\omega^p = P_\omega - \epsilon_\omega + D_{\mathrm{cd}} + \chi f_{b2} f_{b3,lR} P_{\omega,4} \tag{32}$$

with $P_{\omega,4} = C_{\omega 4} P_\omega$. The function $\chi = \chi(\Delta p_s^+, u_\tau/U_e)$ is one if $\Delta p_s^+ > \Delta p_0^+$ and $u_\tau/U_e > 0$, and is zero otherwise. The sign of u_τ/U_e is obtained from the scalar product of the velocity vector at the first node above the wall and at the boundary layer edge [see Cousteix and Houdeville (1981)] and is used to exclude regions of separated flow. The value $\Delta p_0^+ = 8 \times 10^{-6}$ is used. Hence the extra term is not active in favourable pressure gradient (FPG) regions of any flowfield. The calibration of $C_{\omega 4} = 0.335$ instead of $C_{\omega 4} = 0.5$ is mainly based on the DLR/UniBw experiment (see Sect. 7).

5.5 Discussion

A short discussion is dedicated to the modelling assumption (16) and a possible extension of the modification for FPGs.

Consider assumption (16) within the framework of a DRSM (10). Note that, in generalizing the model, P_ω and $P_{\omega,4}$ are computed from P_k. In order to illustrate two aspects of the orientation of the Reynolds stress tensor, $P_{\omega,4}$ is written in a wall- and flow-fitted coordinate system as

$$P_{\omega,4} = C_{\omega 4}\gamma \frac{\omega}{k} P_k = C_{\omega 4}\gamma \frac{a_{12}\omega}{|\overline{u'v'}|} \underbrace{\frac{-\overline{u_i'u_j'}\, \partial U_i/\partial x_j}{\mathcal{RS}}}_{a_{12,\mathrm{prod}}} \mathcal{RS} \tag{33}$$

with $\mathcal{S} = \sqrt{2S_{ij}S_{ij}}$, $S_{ij} = \left(\partial U_i/\partial x_j + \partial U_j/\partial x_i\right)/2$ and $\mathcal{R} = \sqrt{\overline{u_i'u_j'}\,\overline{u_i'u_j'}}$. For comparison, the Boussinesq assumption would imply $P_{\omega,4} = C_{\omega 4}\gamma\mathcal{S}^2$. On the one hand, the orientation of the Reynolds stress tensor in the Bradshaw assumption is related to the mean-velocity vector and a wall-fitted coordinate system [see Coleman et al. (2018)]. This concerns a_{12} in (16), which appears in (33). Subtle changes of a_{12} are found depending on whether u' is defined in the wall-parallel direction or in the direction of the local mean-velocity vector. On the other hand, $a_{12,\mathrm{prod}}$ accounts for the level of alignment between the Reynolds stress tensor and the strain-rate tensor. Following Coleman et al. (2018), $|\tau_{\mathrm{prod}}|/\rho = P_k/\mathcal{S}$ can be called the 'productive stress'. For the DLR/UniBw TBL flow considered in Sect. 7, a small reduction of a_{12} by less than around 10% was observed in the inner layer, in conjunction with an increase of $a_{12,\mathrm{prod}}$ by less than around 15%. Hence, these effects mutually nearly cancel out. This is in concurrence with the notion that a_{12} cancels out in (27). Thus, the net effect discussed using (33) is much smaller than the term $P_{\omega,4}$.

In FPG regions, the modification is deactivated due to the blending functions. One might ask about the idea that the effect of a mild FPG is opposite to a weak APG. However, the data in the literature for the mean-velocity profile do not give a conclusive picture. For the sink flow experiments by Jones et al. (2001), the mean-velocity profiles were found to collapse onto the conventional log law (with $\kappa = 0.41$ and $B = 5.0$). Regarding the outer layer and the law-of-the-wall/law-of-the-wake, the Coles wake factor Π was found to decrease with increasing acceleration parameter $K_{\mathrm{acc}} = \nu U_e^{-2}(\mathrm{d}U_e/\mathrm{d}s)$. On the other hand, Dixit and Ramesh (2008) report an increase of κ up to $\kappa = 0.5$ for the highest level of K_{acc} for their sink flow experiments, which were at larger K_{acc} and at lower Re_τ than the experiments by Jones et al. (2001). An increase of κ was also reported for the experiments by Joshi et al. (2014). Moreover, a downward turn of the mean-velocity profile below the log law might also be observed in figure 6 in Joshi et al. (2014) in the inner layer, in addition to a reduction of Π in the outer layer. Qualitatively, this could be described by (4) using a suitable $\alpha^+ < 0$. Such a downward turn could be an FPG effect opposite to the upward turn above the log law associated with the half-power law for $\alpha^+ > 0$ in an APG [see Knopp et al. (2021)], but it could also be a history effect, given the findings in Jones et al. (2001) (note that the sink flow is an equilibrium TBL). To summarize, the question of the extension of the APG modification for FPG remains open due to the lack of data from experiment or DNS to develop a quantitative model.

6 Numerical Method

The numerical simulations are performed using the DLR TAU-code, the unstructured solver for the compressible RANS equations developed at DLR. The inviscid fluxes are calculated by a second-order central method with artificial matrix-valued dissipation [see Schwamborn et al. (2006)].

For the evaluation of (9), f_{b2}, $f_{b3,IR}$, and χ, an extended data structure within TAU is used [see Knopp and Probst (2013)]. A list of all field points lying on an approximately wall-normal line is provided for each discretisation point at a viscous wall. Additionally,

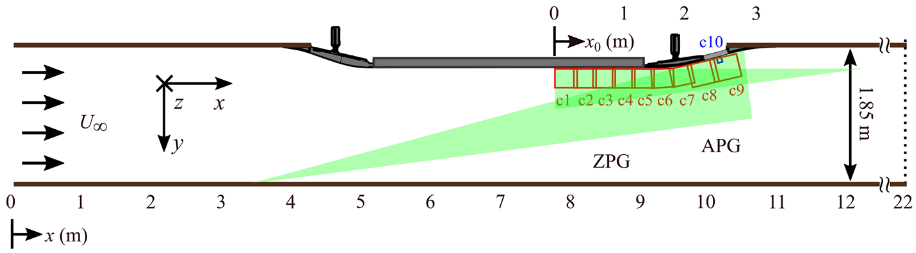

Fig. 4 DLR/UniBw experiment II: Top-down view of the AWM test section with the model installed on the side wall and field of view of the PIV measurement

for each field point, the relevant surface data at the nearest wall point are available. Then surface data like u_τ or Δp_s^+ can be prolongated into the field along the wall-normal lines.

Moreover, this data structure enables the computation of the boundary layer thickness δ for each wall node. Different methods for the determination of δ are provided. Here, $\delta = \delta_{99}/0.94$ is used (see Sect. 2). The boundary layer edge velocity U_e used to determine δ_{99} is approximated using the compressible form of the Bernoulli equation and inviscid theory of isentropic flow [see Krimmelbein (2021)]

$$\frac{U_e}{U_\infty} = \left[1 + \frac{2}{(\gamma - 1)Ma_\infty^2}\left(1 - \left(\frac{P_e}{P_\infty}\right)^{(\gamma-1)/\gamma}\right)\right]^{1/2}. \tag{34}$$

Here, the subscript ∞ denotes values at the farfield or at a reference position, subscript e denotes values at the boundary layer edge, Ma is the Mach number, and γ is the ratio of the heat capacity at constant pressure to the heat capacity at constant volume. Finally, P_e is approximated by the value of P at the corresponding wall node from boundary layer theory. The reason for using (34) is that for the flow around airfoils and airplane wings the boundary layer edge velocity U_e is often neither constant above the boundary layer edge nor given by a distinct velocity maximum [see Vinuesa et al. (2016)].

For internal flows, the maximum velocity along a wall-normal line is used instead of (34). This was found to be a reasonable approximation also for flows with convex streamwise surface curvature [see Knopp et al. (2021)]. For flows with confluent (merging) viscous layers (e.g., the confluent boundary layer and wake flow above the flap of a three-element airfoil), (34) was found to be suitable. For strong merging, $\max(\delta, 0.1c)$ with c being the streamwise length of the nearest surface element (e.g., the flap chord) can be used as a limiter.

7 DLR/UniBw Experiment II

The modification of the SSG/LRR-ω model was calibrated mainly using the joint DLR/UniBw experiment II. The experiment aimed at achieving an attached turbulent boundary layer flow remote from separation at Δp_s^+-values larger than 0.01 for high Reynolds numbers and is used to calibrate $C_{\omega 4}$.

Table 2 Flow parameters of the DLR/UniBw turbulent boundary layer experiment II

U_∞ m/s	x m	U_e m/s	Re_θ	δ_{99} mm	δ^* mm	H_{12}	u_τ m/s	Δp_s^+	β_{RC}
23	8.120	28.13	24358	147.6	16.77	1.250	0.977	−0.00015	−0.156
23	9.944	25.50	39822	203.7	36.96	1.530	0.528	0.0185	27.06
36	8.120	43.29	35908	142.2	16.06	1.247	1.433	−0.00011	−0.167
36	9.944	39.18	57363	192.9	34.54	1.520	0.795	0.0114	26.37

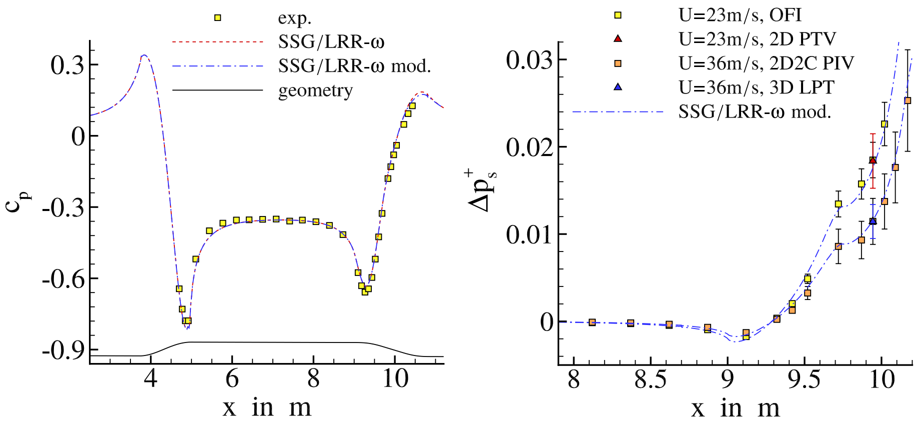

Fig. 5 Streamwise distribution of c_p for $U_\infty = 23\,\mathrm{m/s}$ (left) with the geometry model included (black line, axes not to scale) and Δp_s^+ for $U_\infty = 23\,\mathrm{m/s}$ and $36\,\mathrm{m/s}$ (right)

7.1 Experimental Set-Up and Flow Conditions

The experiment was performed in the atmospheric wind tunnel (AWM) of UniBw München. The test section is 22-m-long and has a rectangular cross section of $1.85\,\mathrm{m} \times 1.85\,\mathrm{m}$. The side walls are at a very small divergence angle to achieve a zero-pressure gradient in the empty test section (both side walls are at an angle of 0.12° with respect to the centerplane). The contour geometry model was mounted vertically. A top-down view of the AWM test section with the model installed on the side wall is depicted in Fig. 4. Note that x is the coordinate parallel to the floor of the wind tunnel, y is the wall-normal coordinate, and z is the spanwise coordinate.

The top and bottom wall of the wind tunnel are parallel. The origin $x = 0$ is defined at the nominal beginning of the test section. The reference position is at $x = 8.12\,\mathrm{m}$ on the 4 m long flat plate in the ZPG region. Then the flow enters the pressure gradient region. The pressure gradient is first favourable and then adverse [see Fig. 5(left)]. On the curved wall segment ($8.99\,\mathrm{m} < x < 9.75\,\mathrm{m}$), the values for δ/R_c are up to 0.06, which is larger than the value of 0.01 associated with mild curvature in the literature, with R_c being the radius of curvature. The focus region is on the inclined flat plate of length 0.4 m, beginning at $x = 9.75\,\mathrm{m}$, at an opening angle of $\alpha = 14.4°$ with respect to the 4.0 m long flat plate. For details see Reuther (2019), Knopp et al. (2021) and Knopp et al. (2022).

The joint measurements by DLR and UniBw München provide a large-scale overview 2D2C-PIV measurement from $x = 7.92\,\mathrm{m}$ to $x = 10.2\,\mathrm{m}$ for the flow field in the two-dimensional plane in streamwise and wall-normal direction for the corresponding two velocity components [see Reuther (2019)]. The field of view (FOV) starts at $x = 7.92\,\mathrm{m}$ (denoted by $x_0 = 0$ in Fig. 4) and includes the overlapping views of nine cameras (c1 to c9). The detailed measurement position in the APG section at $x = 9.944\,\mathrm{m}$ is denoted by c10. Two evaluation methods were used for the 2D2C-PIV data, i.e., a window-correlation method and a single-pixel method. Very accurate measurements down to the wall were accomplished at the APG focus position $x = 9.944\,\mathrm{m}$. At this position, a high magnification long-range microscopic PTV (2D-μPTV) was applied for the case $U_\infty = 23\,\mathrm{m/s}$. The 3D Lagrangian particle tracking (LPT) technique using the Shake-The-Box (STB) method was applied for the case $U_\infty = 36\,\mathrm{m/s}$ to provide all three components of the velocity.

The wall-shear stress was determined from oil film interferometry (OFI) for the case $U_\infty = 23\,\mathrm{m/s}$. Additionally, u_τ was determined from the 2D μPTV data and from the 3D LPT data using an (almost) direct method [see Knopp et al. (2021)]. Moreover, u_τ was determined from the 2D2C PIV data using the standard Clauser chart method. An ad-hoc correction of the standard Clauser chart method for u_τ in the strong APG region was used, based on a correction factor of 1.08 for the case $U_\infty = 23\,\mathrm{m/s}$ and 1.04 for the case $U_\infty = 36\,\mathrm{m/s}$, calibrated by comparison between the value from the standard Clauser chart applied to the 2D2C-PIV data and the (almost) direct method applied to the high-resolution data at $x = 9.944\,\mathrm{m}$. Note that the correction accounts for both the uncertainty of the standard Clauser chart in a strong APG and the uncertainty of the 2D2C-PIV data for $y^+ < 250$ due to the spatial resolution. The estimated relative uncertainties in u_τ are 2% for OFI, 4% for the (almost) direct method using the 2D μPTV and the 3D LPT data, and 6% for the Clauser chart.

The flow conditions at the reference position in the ZPG region $x = 8.12\,\mathrm{m}$ and at the APG focus position $x = 9.944\,\mathrm{m}$ are summarised in table 2. Here, U_∞ denotes the nominal reference velocity measured near $x = 0$, and U_e denotes the boundary layer edge velocity.

Note that the flow remains attached with c_f significantly larger than zero, as inferred from the 2D2C PIV data. There were no indications for corner flow separation in the junction of the contour model and the wind-tunnel side wall from tuft flow visualisation.

The pressure coefficient $c_p = (p - p_\mathrm{ref})/q_\mathrm{ref}$ is depicted in Fig. 5(left). For the dynamic pressure $q_\mathrm{ref} = \rho_\mathrm{ref} U_\mathrm{ref}^2/2$, $U_\mathrm{ref} = U_\infty$ is used. In the APG region, $\mathrm{d}c_p/\mathrm{d}s > 0$ and $\mathrm{d}^2 c_p/\mathrm{d}s^2 > 0$ for $x < 9.7\,\mathrm{m}$, whereas $\mathrm{d}c_p/\mathrm{d}s > 0$ and $\mathrm{d}^2 c_p/\mathrm{d}s^2 < 0$ for $x > 9.7\,\mathrm{m}$. The streamwise evolution of Δp_s^+ is shown in Fig. 5(right). The prediction of the modified SSG/LRR-ω model is included.

7.2 RANS Simulations and Computational Set-Up

The test-case was studied as a 2D case. Initial simulations used the original geometry of the wind tunnel including the nozzle for $x < 0$. The boundary layer thickness predicted by different standard RANS models was found to be significantly smaller than in the experiment [see Knopp et al. (2022)]. Therefore, the computational domain was altered, i.e., the wind-tunnel nozzle was removed and the divergent walls were extended up to $x = -6.2\,\mathrm{m}$. The latter was the result of a number of additional precursor simulations to match the experimental data for the displacement thickness δ^*, the momentum-loss thickness θ, and the shape factor $H_{12} = \delta^*/\theta$ at $x = 8.12\,\mathrm{m/s}$ for the SA and SSG/LRR-ω model.

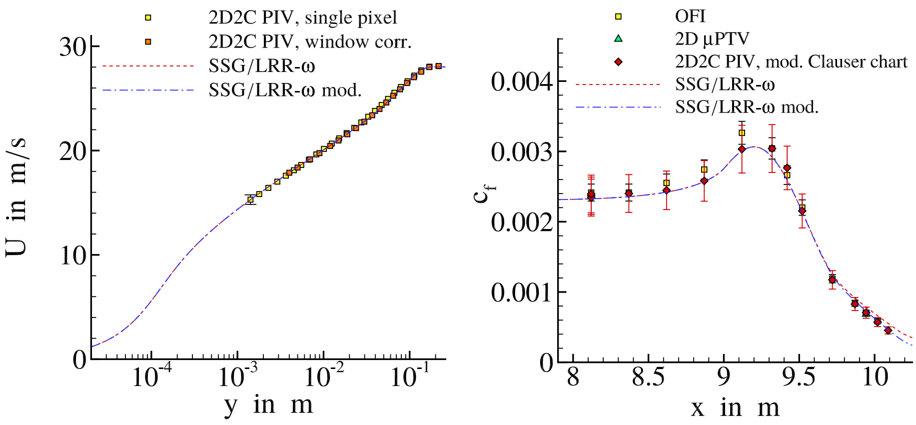

Fig. 6 Case $U_\infty = 23\,\mathrm{m/s}$. Mean velocity at $x = 8.12\,\mathrm{m}$ at the ZPG reference position (left) and c_f-distribution (right)

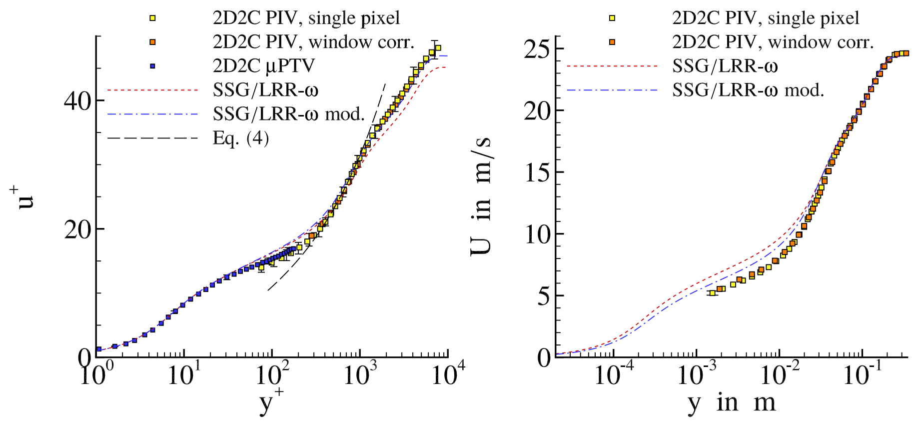

Fig. 7 Case $U_\infty = 23\,\mathrm{m/s}$: Mean-velocity profile in the adverse-pressure-gradient region at $x = 9.944\,\mathrm{m}$ in viscous units (left) and in dimensional units at $x = 10.09\,\mathrm{m}$ (right)

The meshes were generated using the mesh generation tools CentaurSoft and Pointwise. The boundary layers were resolved using up to 167 layers of quadrilateral elements. Outside the boundary layers triangular elements were used. On the finest mesh, the first mesh point above the wall was at $y^+(1) < 0.15$ for $U_\infty = 36\,\mathrm{m}$, and 1836 surface points were used along the wind tunnel wall from $x = -6.2\,\mathrm{m}$ to $x = 15.85\,\mathrm{m}$. In the focus region with surface curvature and adverse pressure gradient from $x = 8.99\,\mathrm{m}$ to $x = 10.19\,\mathrm{m}$, the wall parallel spacing was $\Delta s = 5\,\mathrm{mm}$ on the finest mesh G4. For a mesh refinement study, a series of four meshes G1, G2, G3, and G4 was built (G1 being the coarsest mesh and G4 being the finest mesh level) using a refinement factor of $2^{1/2}$ in wall-parallel and wall-normal direction. For a systematic grid refinement, G2 and G4 lie on top of each other, mesh G4 bisecting each cell face of G2. The level of grid convergence was found to be adequate already for G3. All results are shown for G4.

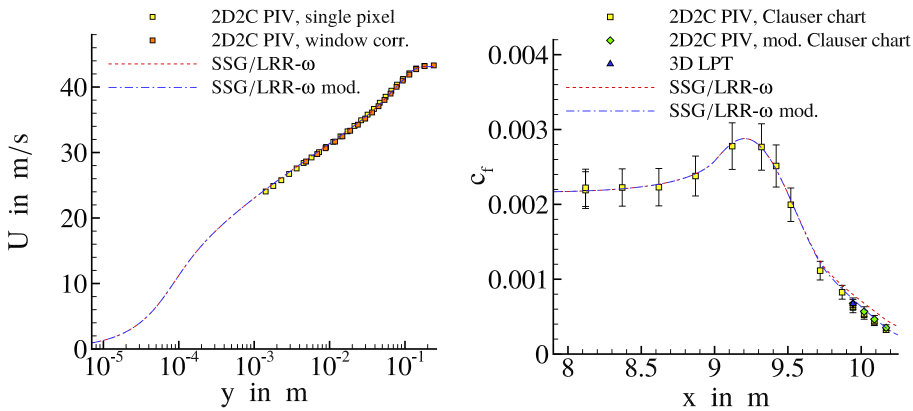

Fig. 8 Case $U_\infty = 36\,\mathrm{m/s}$: Mean velocity at $x = 8.12\,\mathrm{m}$ (left) and distribution of c_f (right)

7.3 Results for the Case $U_\infty = 23\,\mathrm{m/s}$

The results for the case $U_\infty = 23\,\mathrm{m/s}$ are presented first. The mean velocity at the ZPG position $x = 8.12\,\mathrm{m}$ is shown in Fig. 6(left). The modified set-up gives a good agreement of the mean velocity in the inner and outer part of the boundary layer.

The streamwise distribution of the skin friction coefficient $c_f = 2u_\tau^2/U_{\mathrm{ref}}^2$ is shown in Fig. 6(right), using $U_{\mathrm{ref}} = U_{\mathrm{e}}$ at $x = 8.12\,\mathrm{m}$ for non-dimensionalisation. The modification leads to a slight reduction of c_f for $x > 9.6\,\mathrm{m}$ compared to the SSG/LRR-ω model, resulting in a better agreement with the experimental data.

The profile u^+ versus y^+ at $x = 9.944\,\mathrm{m}$ in the APG region is shown in Fig. 7(left). The modification improves the agreement with the experimental data for $y^+ > 700$. The reference solution (4) is also shown. Figure 7(left) illustrates the importance of the structure of the wall law (2), using (3) in the log-law region, in agreement with the work by Perry et al. (1966). It can be seen that (4) is not suitable to describe the mean velocity profile in the entire inner layer above the buffer layer (say, for $100 \leq y^+ \leq 0.2\delta^+$) for large values of Δp_s^+, in contrast to the results for small values of Δp_s^+ by Szablewski (1960). The (formal) interpolation between the log law and the half-power law in (4) cannot describe the resilience of the log law below $y^+_{\mathrm{log,max}}$ for large values of Δp_s^+. Therefore, (4) is used only in the half-power law region in (2).

The experimental uncertainty bars are included. The contribution due to the uncertainty in u_τ by OFI is 2.0%. The uncertainty in U for the 2D μPIV data is around 1.0%. The uncertainty in U for the 2D2C PIV data due to the spatial resolution is estimated to be 3.3% for $y^+ < 400$ and 1% otherwise.

The mean velocity at $x = 10.09\,\mathrm{m}$ is shown in Fig. 7(right). The SSG/LRR-ω model is observed to predict a too high mean velocity in the inner part of the boundary layer for $y < 0.02\,\mathrm{m}$, corresponding to $y \lessapprox 0.1\delta_{99}$. The modification reduces the mean velocity in this region.

Finally, the two-dimensional computational set-up is assessed. The displacement effect of the boundary layers on the spanwise walls in the three-dimensional wind tunnel on the flow in the centerplane is estimated to be small. For a first quantification, two-dimension simulations in the centerplane and three-dimensional simulations of the full test section using the SST k–ω model were compared. While both simulations have the same value of

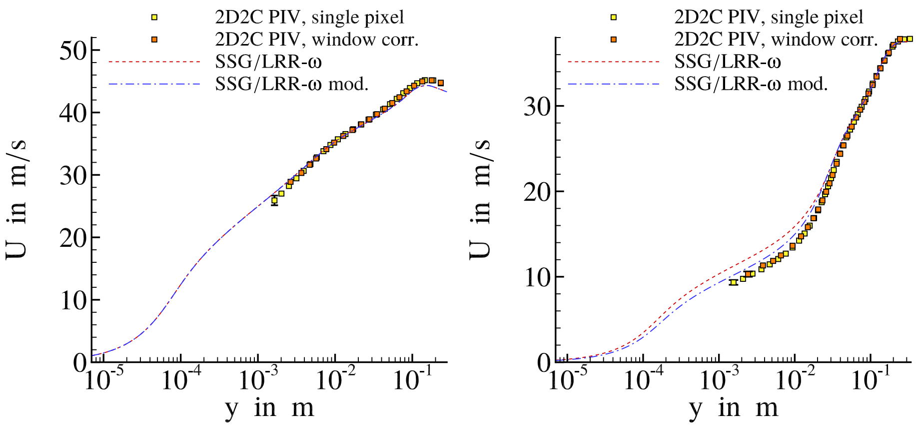

Fig. 9 Case $U_\infty = 36\,\mathrm{m/s}$: Mean velocity at $x = 9.42\,\mathrm{m}$ in the region of convex surface curvature (left) and at $x = 10.09\,\mathrm{m}$ in the APG region (right)

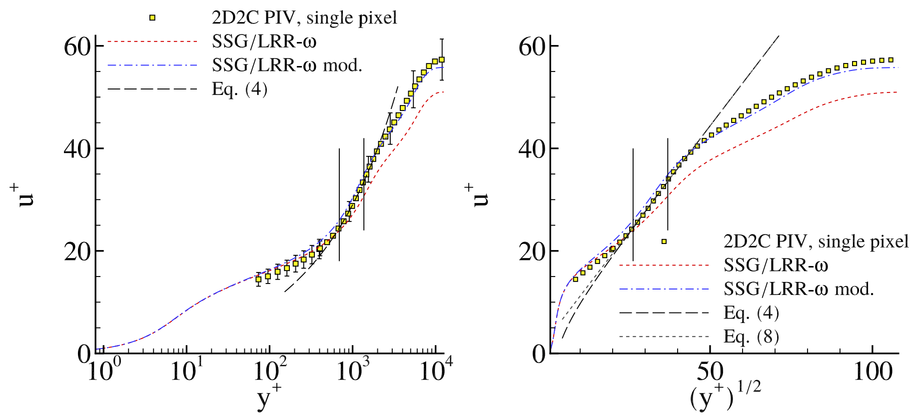

Fig. 10 Case $U_\infty = 36\,\mathrm{m/s}$: Mean velocity at $x = 10.09\,\mathrm{m}$ in viscous units plotted versus $\log(y^+)$ (left) and versus $\sqrt{y^+}$ (right)

U_e in the centerplane at $x = 8.12\,\mathrm{m}$ in the ZPG region, U_e was found to be only 0.6% larger for the 3D simulation at $x = 9.944\,\mathrm{m}$ in the APG regions. Thus the displacement effect of the spanwise side walls is estimated to be small. However, the effect of induced 3D secondary flows due to the adverse pressure gradient cannot be estimated from this.

7.4 Results for the Case $U_\infty = 36\,\mathrm{m/s}$

For the case $U_\infty = 36\,\mathrm{m/s}$, the mean velocity profile at $x = 8.12\,\mathrm{m}$ is shown in Fig. 8(left). The skin friction coefficient $c_f = 2u_\tau^2/U_{\mathrm{ref}}^2$ is shown in Fig. 8(right), using $U_{\mathrm{ref}} = U_{\mathrm{e}}$ at $x = 8.12\,\mathrm{m}$ for non-dimensionalisation. The modification yields a slight reduction of c_f for $x > 9.6\,\mathrm{m}$ compared to the original model, improving the agreement with the experimental data.

The mean velocity in the region of convex surface curvature at $x = 9.42\,\mathrm{m}$ is depicted in Fig. 9(left). A small overprediction of the mean velocity in the inner layer by the SSG/LRR-ω model is observed, indicating that the SSG/LRR-ω model might need a small modification to account for the effects of mild streamwise convex curvature in wall-bounded flows.

The mean velocity at $x = 10.09\,\mathrm{m}$ in the APG region is shown in Fig. 9(right). The SSG/LRR-ω model is observed to predict a too large mean velocity in the inner layer for $y < 0.015\,\mathrm{m}$, corresponding to $y \lessapprox 0.08\delta_{99}$. The modification reduces the mean velocity in this region.

The profile for u^+ at $x = 10.09\,\mathrm{m}$ is shown in Fig. 10(left). The experimental uncertainty bars have a relative magnitude of 9.3% for $y^+ < 400$ and 7% otherwise due to an uncertainty of 6% in u_τ and of 3.3% resp. 1% in U. The reference solution (4) is included together with the half-power law region, which is indicated by the vertical solid lines.

The profile for u^+ versus $\sqrt{y^+}$ is shown in Fig. 10(right). The reference solution (4) is included. Moreover, (8) is plotted. For $y^+ > y^+_{\mathrm{sqrt,min}}$, the curves for (4) and (8) collapse and yield a straight line, showing that for large y^+ and Δp_s^+, (4) asymptotes to (8). The modification improves the agreement with (4) and (8) in the half-power law region.

The choice of the calibration coefficient $C_{\omega 4} = 0.335$ in (32) was a compromise aiming to match (i) the mean velocity profiles in the APG region, (ii) the profiles for u^+ versus y^+, and (iii) the c_f-distribution for both Reynolds numbers. Regarding (i), a small overprediction of the mean velocity in the inner layer by the SSG/LRR-ω model at the upstream position $x = 9.42\,\mathrm{m}$ probably due to the effects of mild streamwise curvature was considered. The deviation of $C_{\omega 4}$ from its theoretical value can be explained by the various modelling approximations used and the design of the blending function $f_{b2} f_{b3}$. The blending function uses a numerics friendly transition between zero and one. As the modification term is partially activated below and above the half-power law region, the lower value of $C_{\omega 4} = 0.335$ is plausible.

8 Two-Dimensional Airfoil Flows

For the further assessment and validation, two-dimension airfoil flows near maximum lift are considered. Cases with incipient separation are of main interest, so that wind-tunnel effects can be expected to be acceptably small.

8.1 NACA 4412 Airfoil at $Re_c = 1.64 \times 10^6$

For the flow around the NACA 4412 airfoil at $Re_c = 1.64 \times 10^6$ and $Ma = 0.085$, the flow conditions are matching the wind-tunnel experiment by Wadcock (1987). The Reynolds number $Re_c = U_\infty c/\nu$ is based on the airfoil chord length c. Boundary layer trips were mounted on both the upper and the lower surface of the airfoil. The RANS simulations used a prescribed transition location from laminar to turbulent flow at $x_{\mathrm{tr}}/c = 0.023$ on the upper side and at $x_{\mathrm{tr}}/c = 0.1$ on the lower side at the same positions as in the experiment by Wadcock (1987).

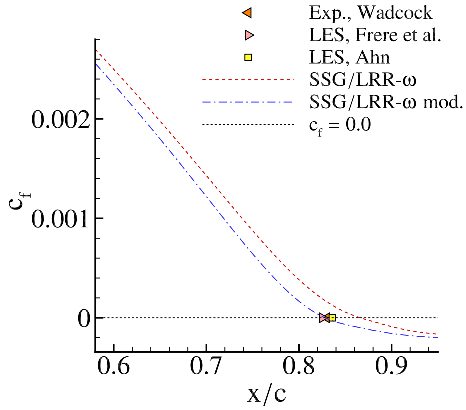

Fig. 11 Distribution of c_f for the NACA 4412 airfoil at $Re = 1.64 \times 10^6$, $\alpha = 12°$

The results shown are for the second finest mesh (897×257 points) of the C-grid family provided by NASA[2] with the medium mesh G3 (449×129 points), the fine mesh G4 (897×257 points), and the very fine mesh G5 (1793×513 points). G4 uses around 256 points on the upper side and the same number on the lower side, and the first point is at $y^+(1) < 0.3$ for most of the airfoil surface, yielding adequate mesh convergence.

The predicted separation point x_{sep}/c for $\alpha = 12°$ is shown in Fig. 11. In the experiment by Wadcock (1987), separation was reported to occur downstream of the position $x/c = 0.815$, where laser-velocimetry data of the velocity were taken, and a value of $x_{\mathrm{sep}}/c = 0.83$ is used here. For the LES by Frere et al. (2018), a relatively large zone of c_f near zero was observed for $x \geq 0.76$. From the mean velocity U, the near-wall flow showed $U > 0$ at $x/c = 0.80$ and $U < 0$ at $x/c = 0.85$. A value of $x_{\mathrm{sep}}/c = 0.825$ is used. A value of $x_{\mathrm{sep}}/c = 0.836$ was found in the LES by Ahn (2014).

The lift coefficient C_L versus α is found to be effected by the details of the prescribed transition location. The choice for x_{tr}/c has a significant effect on the small laminar separation bubble in the RANS results and on C_L for $\alpha > 12°$. For these reasons, the results for C_L are not shown here.

8.2 HGR01 Airfoil at $Re_c = 0.65 \times 10^6$

The flow around the tailplane research airfoil HGR01 is at Reynolds number $Re_c = 0.65 \times 10^6$ and Mach number $Ma = 0.07$. This airfoil was studied experimentally in the low-speed wind tunnel of the Institute of Fluid Mechanics at the Technical University Braunschweig [see Wokoeck et al. (2006)]. It is worthwhile recalling that, in the region of the trailing edge separation, the oilfilm visualisation revealed mushroom shaped three-dimensional structures for $\alpha \geq 12°$, as well as a spanwise variation of the separation line [see Wokoeck et al. (2006), Francois (2014)]. Results from a large-eddy simulation (LES) by Geurts et al. (2012) and from a hybrid RANS/LES simulation (denoted by JHh-RSM ADDES + ST as described in Sect. 8.3) are included for comparison. In the experiments, the transition from laminar to turbulent flow on the upper airfoil side was due to a

[2] https://turbmodels.larc.nasa.gov/naca4412sep_auxgrids.html.

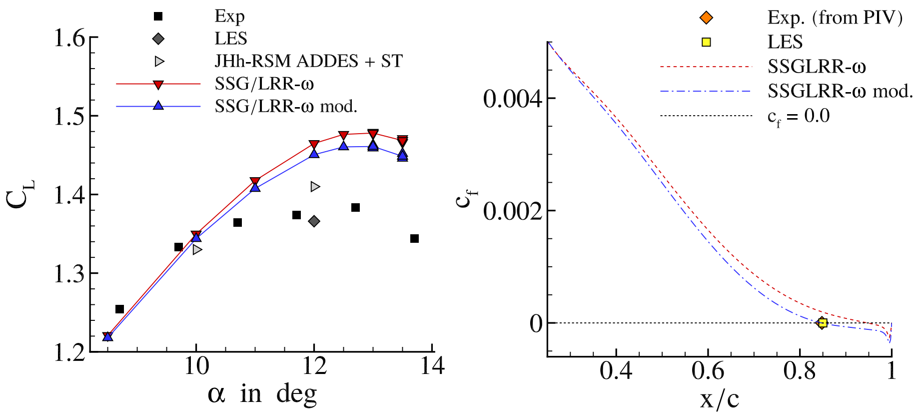

Fig. 12 HGR01 airfoil at $Re_c = 0.65 \times 10^6$: C_L vs. α (left) and c_f for $\alpha = 12°$ (right)

thin laminar separation bubble extending from $x/c = 0.005$ to $x/c < 0.02$ for $\alpha \geq 11°$. In the RANS simulations, transition was prescribed at $x/c = 0.002$ on the upper side and at $x/c = 0.95$ on the lower side.

The meshes were built using the mesh generation tool Pointwise. The boundary layers and the airfoil wake flow were resolved using quadrilateral elements. Outside, triangular elements were used. The mesh resolution is similar to the NACA 4412 mesh G4 [see Francois (2014)].

The results for the lift coefficient C_L versus α are shown in Fig. 12(left). The modified model gives almost the same C_L at $\alpha = 8.5°$ as the original SSG/LRR-ω model, and leads to an increasing reduction of C_L above $\alpha = 10°$ with increasing α. Time-accurate simulations yielded converged values for C_L for $\alpha \leq 12.5°$, but showed a small variability for $\alpha \geq 13.0°$ indicated by the three symbols used in the figure. The prediction for the separation line at $\alpha = 12°$ is shown in Fig. 12(right). The separation point is shifted upstream by the modification, in good agreement with the LES and with the separation point inferred from the PIV data in the centerplane of the wind-tunnel.

8.3 Discussion

The numerical results for the 2D airfoil flows need some discussion. For the HGR01 airfoil, the modified RANS model still overpredicts the lift significantly compared to the reference data. Some concerns regarding the reference data arise. For the LES, the streamwise mesh resolution was only $\Delta x^+ = 100$ and hence coarser than best-practice recommendations used today. More important, the spanwise extent of the computational domain L_z was only a narrow strip ($L_z = 0.02c$). Hence the LES did not capture the large spanwise structures in the separation region.

Regarding the experimental data, it is noteworthy that C_L was obtained by an interpolation of the c_p-distribution. However, the pressure tab resolution was too coarse on the airfoil lower side. Despite these uncertainties in the reference data, the overprediction of C_L is disturbing, as the separation point for the modified RANS model agrees well with the LES and the experimental results. This is probably, at least in part, a failure of the RANS model for the separation region. Hence, the improvement of the RANS model in the attached TBL at APG is not enough. This is supported by the hybrid RANS/LES results

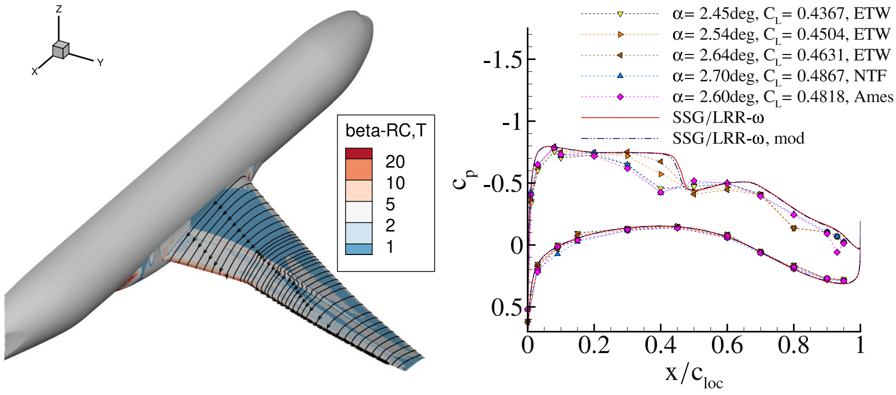

Fig. 13 Demonstration of the applicability of the method for the NASA high speed common research model (CRM) at $M = 0.85$, $Re = 5 \times 10^6$, and $\alpha = 2.5°$

by Francois (2014). The underlying RANS model was a special version of the RSM by Jakirlic and Hanjalic with an APG modification for the ϵ-equation. The boundary layer was computed in RANS mode, and the model switched to the hybrid mode near $x/c = 0.75$. At this position, synthetic turbulence was added over a streamwise distance of around $\delta/2$. The simulation is denoted by JHh-v1 RSM-ADDES + ST ($\delta/2$) in Francois (2014). The results for C_L are closer to the experimental data mainly due to the improved prediction of the separation region.

As a final comment on the use of wind-tunnel data as reference data for subsonic 2D airfoil flows, the flow in the mid-plane of the measuring section is altered not only due to the displacement effect of the boundary layers on the spanwise side walls. Flow separation in the centerplane is likely to be accompanied by corner flow separation at the side walls. Pressure gradients arise not only in the streamwise direction, but also between the airfoil and the opposite wind tunnel wall(s), inducing 3D secondary flows at the side walls. These secondary flows (possibly in conjunction with corner vortices and/or horseshoe vortices) can cause transverse (spanwise) pressure gradients outside the mid-plane. Thus a nominal 2D separation in the mid-plane cannot be investigated without the full 3D flow in the test section. Moreover, the separation line varies in spanwise direction due to the separation at the side walls and due to stall cells. Finally, the lift coefficient near stall can depend crucially on the behaviour of a laminar separation bubble in the leading-edge region and its treatment. To conclude, the use of wind-tunnel data of two-dimensional airfoil flows near maximum lift for the validation (and calibration) of RANS models requires special care.

9 Demonstration for 3D Configurations

The method is workable for 3D configurations. The applicability is demonstrated for the NASA high speed common research model (CRM) used in the 6th and 7th AIAA CFD Drag Prediction Workshop.[3] Test case 3 entitled CRM WB Static Aero-Elastic Effect is considered for $M = 0.85$, $Re = 5 \times 10^6$, and $\alpha = 2.5°$. The wing geometry takes into

[3] https://aiaa-dpw.larc.nasa.gov/Workshop6/workshop6.html.

account the aero-elastic deflections measured in the European Transonic Wind-Tunnel (ETW) test. The simulations used the medium mesh described in Keye and Mavriplis (2017). A parallel computation on 256 subdomains was performed on a high-performance cluster.

The definition of the direction s in $\mathrm{d}P/\mathrm{d}s$ is studied. In a 3D TBL on a swept wing, the mean-velocity vector changes its direction across the boundary layer. Denote $\alpha_{\mathrm{np},0.1\delta}$ the angle between the velocity vector at the first node above the wall (np) and the corresponding field point at wall distance 0.1δ on the wall-normal line. On large part of the wing, $\alpha_{\mathrm{np},0.1\delta} < 5°$. The sensitivity of $\mathrm{d}P/\mathrm{d}s$ on s depends on the cosine of this angle and is thus small.

The pressure gradient parameter $\beta_{\mathrm{RC,T}}$ is shown in Fig. 13(left). Note that $\beta_{\mathrm{RC,T}} = \delta^*/(\rho u_T^2)\mathrm{d}P/\mathrm{d}s$ uses the modified velocity scale u_T instead of u_τ to yield finite values near separation and reattachment. Large parts of the TBL on the wing upper surface are in a mild APG or in a FPG. The wing design of the CRM does not lead to strong APGs. Therefore, it cannot be expected that the APG modification yields large changes of the c_p -distribution. However, such can be expected for a competitive wing design [see Garcia and Ansell (2021)].

The c_p-distribution at a spanwise cut at $\eta = y/b = 0.727$ (b is the wing span) is depicted in Fig. 13(right). The modified model is close to the original model. The shock position is a little more upstream, slightly improving the agreement with the experimental data. For the simulations, the wind-tunnel walls are not used. Farfield boundary conditions are used instead. The wind-tunnel data involve corrections to allow for comparison with free-flight conditions. The corrections are specific for the different wind-tunnels used (ETW, National Transonic Facility (NTF), and NASA Ames transonic wind tunnel). The uncertainties in the computational set-up need to be resolved before the predictive accuracy of the RANS models can be assessed. Ideally, CFD should try to capture all effects in the test-section, including the perforated or slotted walls used in transonic wind tunnels. To conclude, the method is applicable for 3D configurations, leads to a very small improvement for mild APGs, and the modification does not harm the original model.

10 Conclusion

A modification of the RANS turbulence model SSG/LRR-ω based on a new wall law for the mean velocity in an adverse pressure gradient (APG) was presented. The modified model predicts lower values for the mean velocity in the inner part of the boundary layer in an adverse pressure gradient than the original model and is thus more susceptible to flow separation.

The analysis of the ω-equation in the inner layer gives some explanation for the tendency of RANS models based on the ω-equation to predict separation on a smooth surface due to an APG too far downstream, and that this trend is increased for models based on the standard ϵ-equation. The latter can be explained (in part) by the cross-diffusion term arising if the ω-equation is obtained from the ϵ-equation by a variable transformation [see Pope (2000)], as the cross-diffusion term is not used in ω-equation based models in the inner layer.

The method employs functions based on characteristic boundary layer parameters for the local activation of the RANS model augmentation term. The parameters are provided by a data structure of wall-normal lines made available in an unstructured flow solver. This extends the paradigm of RANS modelling for CFD to use only field-point local quantities. The applicability of the method for 3D flows was demonstrated for a wing-body configuration. The boundary layer parameters might also be of interest as flow features for data-driven/machine-learning methods. As a future perspective, the local activation of different augmentation terms depending on the local flow physics could be a way towards an overall improvement of a baseline RANS turbulence model without doing harm in flow regions for which the model is successfully designed for [see Rumsey et al. (2022)]. In this perspective, the present work can be seen as the beginning of a much longer line of work, involving the development of augmentation terms for thin separation regions, wake flows in an APG, and vortical flows.

The calibration of the model was accomplished using a joint DLR/UniBw turbulent boundary layer experiment by balancing the agreement of the mean-velocity profiles (both in dimensional and in viscous units) and the skin-friction coefficient with the experimental data.

The results for 2D airfoil flows near maximum lift confirm the well-known deficiencies of current RANS models for regions of separated flows. The prediction of lift stall shows clear differences compared to the wind-tunnel data, albeit the modified model gives the correct separation point. This yields the idea to use the present modification in a hybrid RANS/LES method to improve the predictive accuracy for separated flow regions.

Another conclusion is that there is still a lack of well-defined test cases for the assessment of flow separation on a smooth surface due to an APG. DNS/LES of a two-dimensional flow using spanwise periodic boundary conditions are limited so far to moderately small *Re*. Wind-tunnel experiments permit higher *Re*, but lead to different uncertainties. Regarding the use of two-dimensional airfoil flows near maximum lift for the validation (and calibration) of RANS models, the need for special care was concluded. Cases with incipient separation were found to be more suitable. The comparison of the separation point between the RANS results and the reference data (from wind-tunnel experiment or LES) is advocated rather than the lift coefficient. This notion might also be of interest for the improvement of RANS models using data-driven/machine-learning methods. Near maximum lift, the behaviour of the lift coefficient is increasingly influenced by the 3D flow in the wind tunnel. Moreover, the laminar separation bubble in the nose region can have a significant effect on the lift coefficient.

For future work, the APG modification will be assessed in detail for industrial aircraft configurations.

Acknowledgements The authors would like to express their gratitude to Andreas Krumbein, Dieter Schwamborn, Cord Rossow, Normann Krimmelbein, Rolf Radespiel, Philippe Spalart, Bertrand Aupoix, Paul Durbin, Florian Menter, Stefan Melber-Wilkending, Stefan Keye, and to the late Bernhard Eisfeld for valuable discussions. Special thanks are to Martin Bitter for his contribution to the design of the DLR/UniBw experiment and to Laura Strampe for her assistence with the mesh generation. Finally, the excellent and very valuable comments and suggestions of the reviewers are gratefully acknowledged.

Author Contributions TK, AS, ES, CJK designed research; TK, NR, MN, D.S, ES, AS, CJK performed research; TK, NR, MN, DS, ES, AS, CJK analysed data; and TK, NR, ES, AS and CJK wrote the paper.

Funding Open Access funding enabled and organized by Projekt DEAL. The experiment was funded within the DFG-project "Analyse turbulenter Grenzschichten mit Druckgradient bei großen Reynoldszahlen mit hochauflösenden Vielkameramessverfahren" (Grant KA 1808/14-1 & SCHR 1165/3-1) and by the DLR Institute of Aerodynamics and Flow Technology. The funding of this work by the DLR internal aeronautical program within the projects VicToria and ADaMant is gratefully acknowledged.

Data Availibility The data could be made available upon reasonable request. This requires permission by DLR.

Declarations

Conflict of interest I declare that the authors have no competing interests as defined by Springer, or other interests that might be perceived to influence the results and/or discussion reported in this paper.

Ethical approval I confirm that the authors have upheld the integrity of the scientific record, thereby complying with the journal's ethics policy.

Informed consent I confirm that all of the material is owned by the authors and/or no permissions from third parties are required.

References

Ahn, E.: Large eddy simulation of flow over NACA4412 airfoil at the critical angle of attack. Technical Report, Master thesis, Seoul University, Department of Mechanical Aerospace Engineering (2014)

Apsley, D.D., Leschziner, M.A.: Advanced turbulence modelling of separated flow in a diffuser. Flow Turbul. Combust. **63**, 81–112 (2000)

Brown, K.C., Joubert, P.N.: The measurement of skin friction in turbulent boundary layers with adverse pressure gradients. J. Fluid Mech. **35**, 737–757 (1969)

Catris, S., Aupoix, B.: Towards a calibration of the length-scale equation. Int. J. Heat Fluid Flow **21**, 606–613 (2000)

Coleman, G.N., Rumsey, C.L., Spalart, P.R.: Numerical study of turbulent separation bubbles with varying pressure gradient and Reynolds number. J. Fluid Mech. **847**, 28–70 (2018)

Coles, D.E., Hirst, E.A.: Computation of Turbulent Boundary Layers—1968 AFOSR-IFP-Stanford Conference. Department of Mechanical Engineering, Stanford University, Stanford CA, Thermosciences Division (1969)

Cousteix, J., Houdeville, R.: Singularities in three-dimensional turbulent boundary-layer calculations and separation phenomena. AAIA J. **19**, 976–985 (1981)

Dixit, S.A., Ramesh, O.N.: Pressure-gradient-dependent logarithmic laws in sink flow turbulent boundary layers. J. Fluid Mech. **615**, 445–475 (2008)

Durbin, P.A., Reif, B.A.P.: Statistical Theory and Modelling for Turbulent Flows. Wiley, Chichester (2001)

Eisfeld, B., Rumsey, C., Togiti, V.: Verification and validation of a second-moment-closure model. AAIA J. **54**, 1524–1541 (2016)

Francois, D.G., Radespiel, R., Probst, A.: Airfoil stall simulations with algebraic delayed DES and physically based synthetic turbulence for RANS-LES transition. AIAA Paper 2014-2574 (2014)

Frere, A., Hillewaert, K., Chatelain, P., Winckelmans, G.: High Reynolds number airfoil: from wall-resolved to wall-modeled LES. Flow Turbul. Combust. **101**, 457–476 (2018)

Garcia, A.R.C., Ansell, P.J.: Design of assisted transonic pressure recovery using passive flow control for airfoil geometries. AAIA J. **60**(4), 2207–2222 (2021)

Geurts, K., Meinke, M., Schröder, W.: A fully coupled zonal RANS-LES method for high angle of attack flow. AIAA Paper 2012-3023 (2012)

Hanjalic, K., Launder, B.E.: Sensitizing the dissipation equation to irrotational strains. J. Fluid Eng. ASME **102**, 34–40 (1980)

Hanjalic, K., Hadzic, I., Jakirlic, S.: Modeling turbulent wall flows subjected to strong pressure variations. J. Fluid Eng. ASME **121**, 57–64 (1999)

Johnstone, R., Coleman, G.N., Spalart, P.R.: The resilience of the logarithmic law to pressure gradients: evidence from direct numerical simulation. J. Fluid Mech. **643**, 163–175 (2010)
Jones, M.B., Marusic, I., Perry, A.E.: Evolution and structure of sink-flow turbulent boundary layers. J. Fluid Mech. **428**, 1–27 (2001)
Joshi, P., Liu, X., Katz, J.: Effect of mean and fluctuating pressure gradients on boundary layer turbulence. J. Fluid Mech. **748**, 36–84 (2014)
Keye, S., Mavriplis, D.J.: Summary of data from the sixth AIAA CFD drag prediction workshop: case 5 (Coupled Aero-Structural Simulation). AIAA Paper 2017-1207 (2017)
Klewicki, J.C., Fife, P., Wei, T.: On the logarithmic mean profile. J. Fluid Mech. **638**, 73–93 (2009)
Knopp, T., Novara, M., Schanz, D., Reuther, N., Lühder, W., Willert, C., Schröder, A., Schülein, E., Hain, R., Kähler, C.J.: Modification of the SSG/LRR-ω RSM for adverse pressure gradients using turbulent boundary layer experiments at high Re. In: 13th International ERCOFTAC Symposium on Engineering Turbulence Modelling and Measurements ETMM13, 15th–17th September 2021, Rhodes, Greece. https://elib.dlr.de/136561/ (2021)
Knopp, T., Probst, A.: An algebraic sensor for the RANS-LES switch in delayed detached-eddy simulation. In: New Results in Numerical and Experimental Fluid Mechanics VIII. Notes on Numerical Fluid Mechanics and Multidisciplinary Design, vol. 121, pp. 457–464. Springer, Berlin (2013)
Knopp, T.A., Schanz, D., Novara, M., Lühder, W., Strampe, L., Schülein, E., Schröder, A., Bross, M., Parikh, A., McLellan, D., Eich, F., Kähler, C.J.: Experimental and numerical investigation of turbulent boundary layers with strong pressure gradients. AIAA Paper 2022-1035 (2022)
Knopp, T.: A new wall-law for adverse pressure gradient flows and modification of k–ω type RANS turbulence models. AIAA Paper 2016-0588 (2016)
Knopp, T.: An empirical wall law for the mean velocity in an adverse pressure gradient for RANS turbulence modelling. Flow Turbul. Combust. **109**, 571–601 (2022)
Knopp, T., Buchmann, N.A., Schanz, D., Eisfeld, B., Cierpka, C., Hain, R., Schröder, A., Kähler, C.J.: Investigation of scaling laws in a turbulent boundary layer flow with adverse pressure gradient using PIV. J. Turbul. **16**, 250–272 (2015)
Knopp, T., Reuther, N., Novara, M., Schanz, D., Schülein, E., Schröder, A., Kähler, C.J.: Experimental analysis of the log law at adverse pressure gradient. J. Fluid Mech. **918**, 17–11732 (2021)
Krimmelbein, N.: Transition prediction method for three-dimensional flows using linear stability theory. Technical report. PhD Thesis, Technische Universität Braunschweig, also DLR-FB-2021-26 (2021)
McDonald, H.: The effect of pressure gradient on the law of the wall in turbulent flow. J. Fluid Mech. **35**, 311–336 (1969)
Medida, S., Baeder, J.D.: Adverse pressure gradient modification to turbulence models for wall-bounded flows. AIAA Paper 2013-2426 (2013)
Mellor, G.L.: The effects of pressure gradients on turbulent flow near a smooth wall. J. Fluid Mech. **24**, 255–274 (1966)
Menter, F.R.: Personal communication (2022)
Menter, F.R.: Zonal two equation k/ω turbulence models for aerodynamic flows. AIAA Paper 1993-2906 (1993)
Menter, F.R., Matyushenko, A., Lechner, R.: Development of a generalized K-ω two-equation turbulence model. In: Dillmann, A., Heller, G., Krämer, E., Wagner, C., Tropea, C., Jakirlic, S. (eds.) New Results in Numerical and Experimental Fluid Mechanics. Contributions to the 21th STAB/DGLR Symposium Darmstadt, Germany 2018, vol. 142, pp. 101–109. Springer, Cham (2018)
Perry, A.E., Bell, J.B., Joubert, P.N.: Velocity and temperature profiles in adverse pressure gradient turbulent boundary layers. J. Fluid Mech. **25**, 299–320 (1966)
Pope, S.B.: Turbulent Flows. Cambridge University Press, Cambrigde (2000)
Probst, A., Radespiel, R.: Implementation and extension of a near-wall reynolds-stress model for application to aerodynamic flows on unstructured meshes. AIAA Paper 2008-770 (2008)
Rao, M.S., Hassan, H.A.: Modeling turbulence in the presence of adverse pressure gradients. J. Aircraft **35**, 500–502 (1998)
Reuther, N.: Impact of the intermittent behavior on statistics in pressure gradient turbulent boundary layers. PhD Thesis. Universität der Bundeswehr München, Fakultät für Luft- und Raumfahrttechnik, Institut für Strömungsmechanik und Aerodynamik (2019)
Rumsey, C.L., Coleman, G.N., Wang, L.: In search of data-driven improvements to RANS models applied to separated flows. AIAA Paper 2022-0937 (2022)
Schwamborn, D., Gerhold, T., Heinrich, R.: The DLR TAU-Code: Recent Applications in Research and Industry. In: Wesseling, P., Onate, E., Periaux, J. (eds.) European Conference on Computational Fluid Dynamics, ECCOMAS CFD 2006. TU Delft, The Netherlands (2006)
Spalart, P.R.: Philosophies and fallacies in turbulence modeling. Prog. Aerosp. Sci. **74**, 1–15 (2015)
Stratford, B.S.: The prediction of separation of the turbulent boundary layer. J. Fluid Mech. **5**, 1–16 (1959)

Szablewski, W.: Analyse von Messungen turbulenter Grenzschichten mittels der Wandgesetze. Ing. Arch. **29**, 291–300 (1960)
Townsend, A.A.: The development of turbulent boundary layers with negligible wall stress. J. Fluid Mech. **10**, 143–155 (1960)
Vinuesa, R., Bobke, A., Örlü, R., Schlatter, P.: On determining characteristic length scales in pressure-gradient turbulent boundary layers. Phys. Fluids **28**, 055101 (2016)
Wadcock, A.: Investigations of low-speed turbulent separated flow around airfoils. Technical Report, NASA Contractor Report 177450 (1987)
Wilcox, D.C.: Turbulence Modeling for CFD. DWC Industries, La Canada (1998)
Wokoeck, R., Krimmelbein, N., Ortmanns, J., Ciobaca, V., Radespiel, R., Krumbein, A.: RANS simulation and experiments on the stall behaviour of an airfoil with laminar separation bubbles. AIAA Paper 2006-0244 (2006)
Yaglom, A.M.: Similarity laws for constant-pressure and pressure-gradient turbulent wall flows. Annu. Rev. Fluid Mech. **11**, 505 (1979)

Authors and Affiliations

Tobias Knopp[1] · Nico Reuther[2] · Matteo Novara[1] · Daniel Schanz[1] · Erich Schülein[1] · Andreas Schröder[1] · Christian J. Kähler[2]

✉ Tobias Knopp
Tobias.Knopp@dlr.de

Nico Reuther
Nico.Reuther@unibw.de

Matteo Novara
Matteo.Novara@dlr.de

Daniel Schanz
Daniel.Schanz@dlr.de

Erich Schülein
Erich.Schuelein@dlr.de

Andreas Schröder
Andreas.Schroeder@dlr.de

Christian J. Kähler
Christian.Kaehler@unibw.de

[1] Institute of Aerodynamics and Flow Technology, Deutsches Zentrum für Luft- und Raumfahrt, Bunsenstr. 10, 37073 Göttingen, Germany

[2] Institute of Fluid Mechanics and Aerodynamics, Universität der Bundeswehr München, Werner-Heisenberg-Weg 39, 85577 Neubiberg, Germany